ACOUSTIC PULSE TIME OF ARRIVAL ESTIMATE BY RISING EDGE DETECTION

by

Brad Albert Delanghe

Bachelor of Applied Science (Electrical Engineering)
University of Waterloo, 1992

A THESIS SUBMITTED IN PARTIAL FULFILLMENT
OF THE REQUIREMENTS FOR THE DEGREE OF
MASTER OF APPLIED SCIENCE
in the School
of
Engineering Science

SIMON FRASER UNIVERSITY
July 8, 1994

APPROVAL

Name: Brad Albert Delanghe

Degree: Master of Applied Science

Title of thesis : Acoustic Pulse Time of Arrival Estimate by Rising Edge Detection

Examining Committee: Dr. John D. Jones
Associate Professor, Engineering Science, Chairman

Dr. John S. Bird
Associate Professor, Engineering Science
Senior Supervisor

Dr. Paul Ho
Associate Professor, Engineering Science
Supervisor

Dr. Jacques Vaisey
Assistant Professor, Engineering Science, P.Eng
Internal Examiner

Date Approved: July 27, 1994

PARTIAL COPYRIGHT LICENSE

Title of Thesis/Project/Extended Essay

"Acoustic Pulse Time of Arrival Estimate"

Author:

(signature)

Brad Delanghe
(name)

July 22, 1994
(date)

Abstract

A simple and novel technique for acoustic pulse timing in reverberant multipath environments has been developed and implemented as part of an underwater acoustic positioning system. The technique fits the rising edge of the incoming pulse using two threshold levels and their corresponding crossing times and was found to give an asymptotically unbiased estimate of the time of flight. The pulse timing system utilizes fast analog electronics and gives results which are superior to the simple threshold crossing method yet without the overhead of a full digital sampling system.

The underwater acoustic transducers used in this thesis were found by experiment to produce pulses having a nearly parabolic rising edge. The two threshold levels and their crossing times were then used in a parabolic fit of the rising edge of the pulse. The choice of these two threshold levels, relative to the signal peak, was investigated. It was found that for minimum error in the fit the lower threshold should be set as low as possible based on the noise level and the upper threshold should be set to between two and four times the level of the lower threshold. Over the range of expected incoming signal levels the time of arrival estimate is accurate to within $\sim \pm 6\mu S$.

Acknowledgements

I would like to express my gratitude to the Natural Sciences and Engineering Research Council and the Advanced Systems Institute for their financial support.

I wish to thank Dr. John Bird for his assistance and guidance through the course of this research. Thanks to all the guys in the URL, Bill McMullan, Paul Kraeutner, Denis Lizandier and Harry Bohm who enlightened me with their words of wisdom and worldly advice.

Finally, I would like to thank my family and my friends, Scott Evenson and Apurva Desai, for their encouragement and support.

for Jack ...

Cheers mate!

Contents

List of Tables

List of Figures

List of Symbols

a curvature parameter used in the rising edge fit

AL attenuation loss, accounts for the loss in intensity due to absorption and is a function of the medium and the frequency of operation

AUV Autonomous Underwater Vehicle

BW equivalent noise bandwidth of the system in Hertz

$\mathbf{C_m}$ compliance of the vibrating mass of the transducer element

$\mathbf{C_0}$ electric "static" capacitance of the transducer element

CPU Central Processing Unit

$\mathbf{\Delta R_{cc}}$ uncertainty in the centre-to-centre transducer separation measurement

$\mathbf{\Delta t}$ uncertainty in the threshold crossing times

$\mathbf{\Delta t_a}$ uncertainty in the time of arrival estimate

$\mathbf{\Delta tof}$ uncertainty in the time of flight measurement

$\mathbf{\Delta v}$ uncertainty in setting the threshold levels

$\mathbf{\Delta v_{sound}}$ uncertainty in the speed of sound

DI directivity index, accounts for the fact that the source does not radiate isotropically

$\eta_{\mathbf{waveform}}$ efficiency of the transmit waveform

$\eta_{\mathbf{xducer}}$ efficiency of the transducer

f frequency in Hertz

$\mathbf{f_o}$ resonant frequency of the transducers in Hertz

$\mathbf{I_{NT}}$ intensity of the acoustic thermal noise

$\mathbf{I_{ref}}$ intensity which results from a plane wave of rms pressure of 1μPa in water

$\mathbf{k_{vp}}$ constant of proportionality which relates the voltage developed across R_{RAD} to the pressure of the outgoing acoustic wave, p_{out}

$\mathbf{k_{pv}}$ constant of proportionality which relates the pressure of the incoming acoustic wave to the voltage appearing at the input terminals of the equivalent circuit model

$\mathbf{l}$ length of the transducer in meters

λ wavelength of the pressure wave in water in meters

$\mathbf{L_m}$ inertia of the vibrating mass of the transducer element

$\mathbf{n}$ order of curve used to fit the rising edge, determined by the shape of the rising edge of the incoming pulse

N-FET control signal which goes to the N-channel MOS-FET

$\mathbf{N_{thermal}}$ acoustic thermal noise in decibels

OCV open circuit voltage, is a measure of the receive sensitivity of the transducer

PC Personal Computer

$\mathbf{P_{false}}$ probability of false alarm

P-FET control signal which goes to the P-channel MOS-FET

$\mathbf{p_{out}}$ pressure of the outgoing acoustic wave

$\mathbf{R_{cc}}$ measured centre-to-centre transducer separation

$\mathbf{R_{LOSS}}$ unwanted heating losses in the piezo-electric transducer material

$\mathbf{R_{RAD}}$ radiation resistance, accounts for the acoustic energy beamed out into the water

ROV Remotely Operated Vehicle

$\mathbf{R_{xducer}}$ impedance of the transducer

SFU Simon Fraser University

σ variance of the noise

SL source level, intensity of a plane wave produced by an acoustic source relative to the reference intensity. The source level takes into account the efficiency of the transducer and the efficiency of the transmit signal waveform

SNR Signal-to-Noise Ratio

$\mathbf{t_a}$ time of arrival estimate

$\mathbf{t_{bias}}$ time bias, consists of the constant system bias, the SNR bias and the parabolic approximation bias. The constant system bias is isolated by minimizing the effects of the SNR level and the parabolic approximation

$\mathbf{t_i}$ time at which the incoming signal exceeded threshold level i

$\mathbf{t_0}$ time at which the incoming acoustic pulse actually arrived

TER lower **T**hreshold level to **E**nvelope peak **R**atio, $TER = \frac{v_1}{V_p}$

TL transmission loss, accounts for the loss in intensity due to spreading

toa time of arrival, the time at which the incoming signal arrived at the receive hydrophone

tof time of flight, the time difference between the transmission of the acoustic pulse and the reception of the acoustic pulse

URL Underwater Research Laboratory

$\mathbf{v_i}$ threshold level i

$\mathbf{V_{in}}$ input voltage across the transducer element

$\mathbf{v_{NRLII}}$ speed of sound estimate using the Naval Research Laboratory II speed of sound model in natural waters

$\mathbf{V_p}$ envelope peak voltage level

$\mathbf{V_R}$ threshold ratio, the upper threshold level relative to the lower threshold level, $V_R = \frac{v_2}{v_1}$

$\mathbf{v_{sound}}$ speed of sound in water in $[\frac{m}{s}]$

$\mathbf{V_{TX}}$ peak transmit voltage

$\mathbf{Z_{RLC}}$ impedance of the resistor, inductor and capacitor (RLC) network

Chapter 1

INTRODUCTION

The boom in manned submersibles for scientific study in the oceans, in the 1970's, was pushed by the advantages obtained by placing the human eye, hand and brain, as well as the instruments, at the point of observation. Treadwell (1977) has stated, "Humans provide the unique capacity for observation and interaction, but in return they require life-support and safety systems which are complex, expensive and non-optional." Advances in computer and sensor technology have removed the need for humans to be present at the point of observation and paved the way for the development of unmanned submersibles.

Remotely operated vehicles (ROV) represent the first generation of unmanned submersibles. With these tethered vehicles instruments are delivered to the point of observation and operations are performed in hazardous areas without endangering human life. ROVs also operate for extended periods of time since both power and communications are transmitted through the umbilical from the surface vessel and vehicle operators are changed as often as necessary without having to interrupt the mission. However, there are problems associated with ROVs. The tethers are long, heavy, very difficult to manage and often quite expensive. They have a tendency to tangle and they also limit the range of operation. The expense of a crew has just shifted from the manned submersible to the surface vessel. For these reasons there has been a concerted effort to develop unmanned, untethered vehicles.

Autonomous Underwater Vehicles (AUVs) are the second generation of unmanned underwater vehicles. These free-swimming, untethered vehicles have eliminated the

expense and limitations of the umbilical cable, but now must deal with the difficulties associated with the loss of communications and power supplied from the surface. AUVs must provide their own power, operate their own sensors and accurately navigate according to a mission plan. Thus, a navigation system consisting of vehicle positioning and a control strategy is requisite.

Great interest has been shown in and much research has been done throughout the world on AUVs in the recent past (Marine Systems Engineering 1993). The Underwater Research Lab (URL) at Simon Fraser University (SFU) has constructed an AUV to use as a test platform in carrying out research on control strategies and positioning, as well as 3-D acoustic bottom imaging. This thesis is concerned with the problem of designing, constructing and implementing a robust positioning system for the URL AUV.

1.1 Overview of Positioning Systems

A positioning system determines the location of an object relative to a known reference. Acoustic object localization systems have a wide range of applications in both air and water. Some applications include imaging, obstacle avoidance, mobile robot positioning (Ullate et al. 1993 and the references contained therein), subsea surveying for mining, drilling and pipe laying (Christensen 1979), bottom profiling and surface and subsea positioning to name only a few.

There are two basic methods by which an object or vehicle can be tracked with a system of receivers depending on whether or not the time at which the vehicle 'pings' (i.e. transmits the pulse) is known. If the ping emission time is known, the absolute range R, but not the bearing, between the pinger and the receiver can be determined. The object is thus known to be located on a sphere of radius R centered on the receiver. The position of the object is then given by the intersection of three such spheres each centered on one of three receivers. This is known as spherical tracking.

Determining the ping emission time is not trivial. There must be some form of synchronization or communication between the pinger and the receivers. This can be a physical connection, which clearly defeats the purpose of an AUV, or some form of synchronized clocks. If there is no synchronization and the ping emission time is unknown, then only the range difference between the pinger and any pair

of receivers can be determined. In this case the positional solution takes the form of intersecting hyperboloids and is called hyperbolic tracking. Milne (1983) has presented an overview of these tracking methods focussing on subsea applications.

For either tracking method, the position can be calculated directly or iteratively (Anderson 1979). If there are an equal number of knowns and unknowns (eg three position coordinates and three receivers), the system is critically determined and the position can be determined uniquely. If, however, there are more knowns than unknowns (eg the problem of four intersecting spheres) the system is over determined and a best fit of the data is usually solved with iterative methods.

Regardless of the tracking method employed, the algorithm applied or the environment involved, the accuracy of the positioning system is a direct function of how accurately the range can be measured. The range is a function of the time-of-flight (tof) and the speed of sound in water. Much research has been done on the factors affecting the sound speed in water (Wilson 1959; Del Grasso 1974; Mackenzie 1981) and will not be considered in this thesis. The thrust of this thesis is to devise and construct a system to accurately determine the time-of-flight in a highly reverberant, multipath environment.

1.2 Time-of-Flight Measurements

The distribution of noise in most acoustic receiver systems can be characterized as zero mean white Gaussian noise. The optimal detector for time of flight measurement under these conditions is the matched filter (Papoulis 1984; Van Trees 1971). Numerous researchers have applied variations of this technique to enhance the accuracy of ultrasonic tof measurements. Parrilla et al. (1991) investigated several digital signal processing algorithms to improve the accuracy of ultrasonic range measurements. Carpenter and Stepanishen (1984) and Ullate et al. (1993) both used deconvolution to remove the effects of the transducer on pulse broadening. The received pulse, after deconvolution, was then match filtered. Takeuchi (1990) used a signal source which was phase-modulated by a maximal-length binary sequence. The key point to note is that all these techniques, and matched filter techniques in general, require integration over the entire duration of the pulse. The requirement of integrating over the entire pulse leads one to question what if the whole clean pulse is not available such as in test

tanks, swimming pools and any other strongly reverberant multipath environments.

Initial research with the URL AUV and its associated subsystems will be carried out primarily in test tanks, swimming pools and other highly reverberant, multipath environments. Since positioning systems ultimately depend on accurately measuring the time-of-flight of a signal pulse, the presence of multiple signal reflections due to reverberation, which can easily corrupt these measurements, greatly increases the complexity of the task. Specifically, this echo interference precludes pulse integration and therefore matched filter techniques cannot be used. Under such highly reverberant conditions one is restricted to determining the time of flight by using only the rising edge of the waveform.

Perhaps the most straightforward method of rising edge detection involves a simple threshold crossing technique. In this method, a threshold is preset at a specific signal level and the time at which the signal rises above this level is used as the time of flight estimate. This type of technique is simple and inexpensive, but is a biased estimator of the time of flight. The bias in the estimate is a function of the signal shape and, more importantly, of the Signal-to-Noise Ratio (SNR). A decreasing SNR results in an increasing bias and, since the SNR is not known, the bias is also not known and cannot be removed.

In order to remove the bias in the estimator, more sophisticated time of flight measurement techniques must be considered. Freitag and Tyack (1993) describe a situation very similar to the AUV positioning problem considered in this thesis. The authors were attempting to track dolphins in both the ocean and in tanks with accuracies of a fraction of a meter. In the tank, they acknowledged that due to multipath only the rising edge could be considered. Freitag and Tyack correlated the received signal with that of the rising edge of a previously sampled version of the dolphin's call. They applied this technique by sampling the dolphin's calls during their observation period then performed post processing of the data. The estimate was made by detecting the first peak in the correlation above a given threshold. The technique increases signal to noise ratio and results in an unbiased estimator, but is not real time. It requires the incoming signal to be sampled and correlated before the first peak of the correlation is detected.

Barshan and Kuc (1992) developed an edge detection scheme while developing an obstacle localization sonar. After careful observation of many experimental pulses

Barshan and Kuc developed a complicated mathematical description of the entire pulse shape, but realized that the lower portion of the rising edge of a received pulse was basically just parabolic. Their technique samples the incoming received signal and fits the lower portion of the rising edge to a parabola which provides a measure of the start time of the pulse and thus an estimate of the time of flight. This technique is an unbiased estimator of the time of flight that uses only the rising edge of the incoming pulse and therefore has some immunity to multipath effects. Their system is in air and thus uses lower frequencies than an underwater system of comparable accuracy. This results in A/D requirements that are much less stringent than an underwater system and allows them to perform their calculations in real time.

Consideration of the above paper led to the realization that the only useful samples are those on the lower portion of the rising edge. Even though the A/D samples the entire pulse, only the samples taken on the lower portion of the rising edge are actually used for tof calculations. Hence there is no loss of accuracy to the parabolic curve fit technique if only samples on the lower portion of the rising edge are taken. It is not strictly necessary to use an A/D converter to obtain the rising edge samples. These sample points can also be obtained using a multiple threshold crossing scheme. Such a threshold crossing system has the advantage that only the useful samples are taken, the complexity (and ultimately cost) of the system is reduced, and the system is fast enough to operate in real time. Thus, if we combine the simple threshold technique and the parabolic fit technique something both simple and useful results: a simple quasi-unbiased estimator of the time of flight where quasi-unbiased suggests that a small bias is seen as a result of the parabolic assumption and SNR effects but it is well within acceptable limits.

1.3 Contributions of the Thesis

The objective of this thesis is to develop a pulse time of arrival measurement technique for use in the AUV positioning system. Because of the nature of the AUV and its missions, the system is required to operate in multipath environments and must not add any substantial CPU demands. The positioning system requires the time of arrival estimate of the range to be within a few centimeters over the range of SNR levels expected during the operation of the AUV.

In this thesis, a technique is developed which fits the rising edge of the incoming pulse by using two thresholds levels and their associated crossing times. The shape of the rising edge is system dependent and, although this positioning system produces pulses with an almost parabolic rising edge, the described technique can be applied equally well to any system where pulses rise as $a(t - t_a)^n$. The technique is implemented simply using fast analog electronics and produces results which are a substantial improvement over the simple threshold crossing technique yet with only very minor additional complexity.

In chapter 2 a novel concept of a quasi-unbiased estimator is presented and developed theoretically. First, the simple threshold detector is shown to have an unacceptable bias for this positioning system. Next, a two point fit of the rising edge is considered as an alternative to using an A/D converter. Two points can be used to fit a curve of the form

$$v = a(t - t_a)^n \tag{1.1}$$

where the order n depends on the shape of the rising edge of the pulse and is determined by examining the equivalent circuit transducer model and a real digitized pulse. The rising edge of the pulse is determined to be almost parabolic. The choice of threshold levels is examined and the parabolic assumption is tested. Finally, the noise characteristics of the system are discussed.

Chapter 3 looks at the Time of Arrival (toa) system hardware. The system is broken down into the major functional blocks, transducers, transmit/receive switch, transmitter, receiver, control logic and timing, and software. These blocks are described and discussed.

The experiments devised in order to characterize the system and to quantify the accuracy of the time of arrival estimate are described and discussed in Chapter 4. The experimental results are analyzed, displayed and compared with theoretical predictions.

Chapter 5 discusses the conclusions of the research.

Chapter 2

THEORY

When performing time of flight measurements in a highly reverberant variable multipath environment, overlapping echoes may preclude the use of matched filtering. A simple alternative technique, which is not as sensitive to multipath interference, is rising edge detection. A simple threshold crossing technique is discussed and shown to have an unacceptable signal level dependent bias that cannot be removed. A method more sophisticated than the threshold crossing technique is then investigated, one that considers the shape of the rising edge of the incoming pulse. Two threshold levels and their associated crossing times are used as samples of the rising edge. These samples are then fit to a curve of the form $v = a(t - t_a)^n$ where n is system dependent. The transducers of the system described in this thesis are modelled using a conventional equivalent circuit model. The model is shown not to hold for the specific transducers used in this thesis but gives a general indication of the shape of the rising edge. A more accurate estimate of the shape of the rising edge is obtained by digitizing a pulse sent through the specific transducers. The rising edge is shown to have an almost parabolic shape and the degree of the parabolic nature over the entire rising edge is investigated to find the best threshold values and threshold ratio. Finally, the effect of noise on the time of arrival measurement is considered.

2.1 Simple Threshold Crossing Technique

In the simple threshold crossing technique, the time of arrival estimate is the time at which the incoming signal exceeds a preset signal level or threshold. The systematic

difference between the time when the pulse actually arrives, t_0, and the estimate of the arrival time, t_a, is called the bias in the estimator as shown in Figure 2.1.

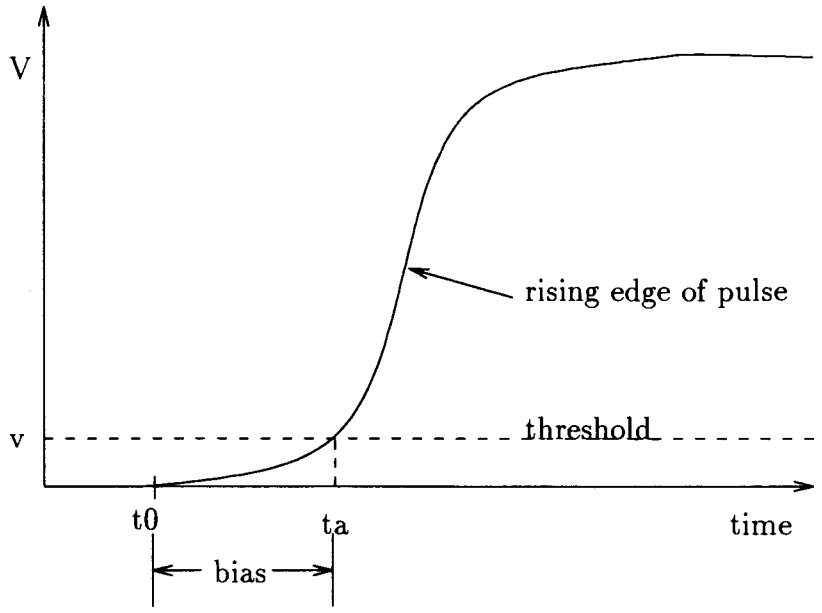

Figure 2.1: The time at which the signal exceeds the threshold level is used as the time of arrival estimate t_a. The systematic difference between the actual time of arrival t_0 and the estimate t_a is the bias in the estimator.

Figure 2.2 shows the rising edge of a pulse with different threshold levels. As can be seen all threshold levels result in a bias in the pulse time of arrival (toa) estimate and different threshold levels produce different biases. Thus, for a constant amplitude pulse, the simple threshold crossing technique results in a threshold level dependent bias.

The bias could easily be removed from the estimate if it were constant. The pulse rise time used in the system is determined primarily by the transducers and electronics and is essentially constant. A consequence of a constant rise time is that the pulse toa estimate will vary as a function of the signal amplitude. This is illustrated in Figure 2.3 which shows a series of constant rise time pulses with a single constant threshold level. For a system where various input signal levels are expected, one can see that the bias associated with the toa estimate will not be constant.

In general the threshold level is set based on the noise level, and since the bias decreases with increasing signal level (Figure 2.3), the bias is a function of the signal

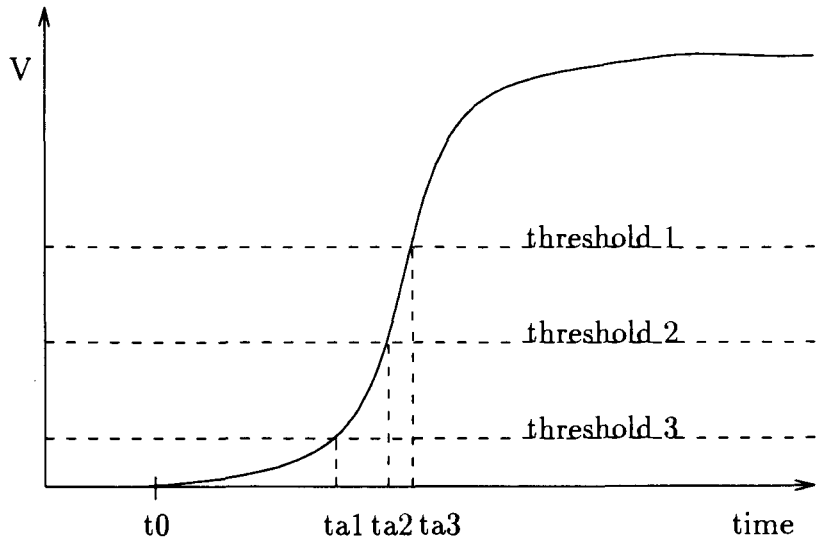

Figure 2.2: The estimate in the time of arrival using a simple threshold technique can be seen to vary with the threshold level. Here three threshold levels result in three different time of arrival estimates t_{a_1}, t_{a_2} and t_{a_3}

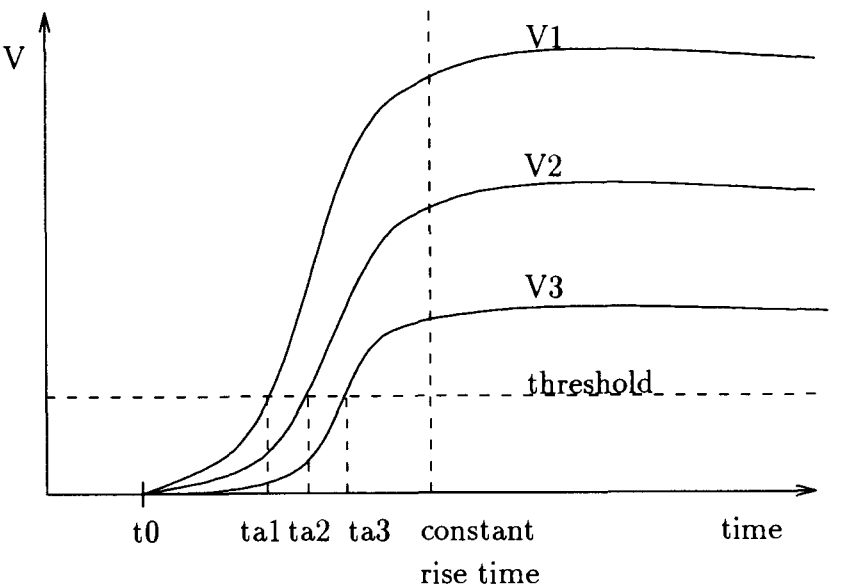

Figure 2.3: The bias in the estimate is also a function of the signal amplitude. For a fixed threshold level, various signal amplitudes result in different time of arrival estimates.

to noise ratio (SNR). If the SNR were sufficiently large, or the rise time of the system were sufficiently small, the bias in the estimate of the time of arrival would be insignificant and could be ignored. In most acoustic applications the low bandwidth of the transducers results in long rise time systems. As will be shown later, the rise time of the system described in this thesis is not sufficiently small and the SNR is not sufficiently high that the bias can be ignored.

2.2 Two Point Fit

If the rising edge of the pulse is to be used in the estimate of the time of arrival, a method more sophisticated than the simple threshold crossing technique must be employed. For example, Barshan and Kuc (1992) used an A/D converter to sample the incoming signal and used the samples on the rising edge in an iterative fit. This requires an A/D converter to sample the entire incoming signal, processing to select appropriate samples for the fitting procedure and more processing for the iterative fit. Note, however, that no loss of accuracy is incurred if the only samples taken are those along the rising edge, since these are the only points used in the fit. A simple, quick and inexpensive method of doing this would be to set multiple thresholds on the rising edge and use the threshold levels and corresponding crossing times as the sample points. This can be performed simply with fast analog electronics and also ensures that only appropriate samples are taken.

An improvement in the accuracy of the time of arrival estimate, over the simple threshold estimate technique, can be obtained by fitting the rising edge with a curve of the form $a(t - t_a)^n$, where a is a curvature parameter and t_a is the time of arrival estimate. The minimum number of points required to fit a curve of this form is two. If only two threshold points are taken the estimate of the arrival time, t_a, can be solved for directly using

$$\begin{aligned} v_1 &= a(t_1 - t_a)^n \\ v_2 &= a(t_2 - t_a)^n \end{aligned}$$

solving for t_a yields

$$t_a = \frac{v_1^{\frac{1}{n}} t_2 - v_2^{\frac{1}{n}} t_1}{v_1^{\frac{1}{n}} - v_2^{\frac{1}{n}}} \tag{2.1}$$

The order of the exponent appearing in (2.1) must now be determined.

Before determining the shape of the rising edge some relevant parameters will be introduced as they will be used throughout this thesis. The threshold ratio is the relationship between the upper threshold level and the lower threshold level ($V_R \equiv \frac{v_2}{v_1}$). The lower Threshold level to Envelope peak ratio, $TER \equiv \frac{v_1}{V_p}$, gives an indication of where the thresholds are on the rising edge of the pulse. These parameters are shown in Figure 2.4.

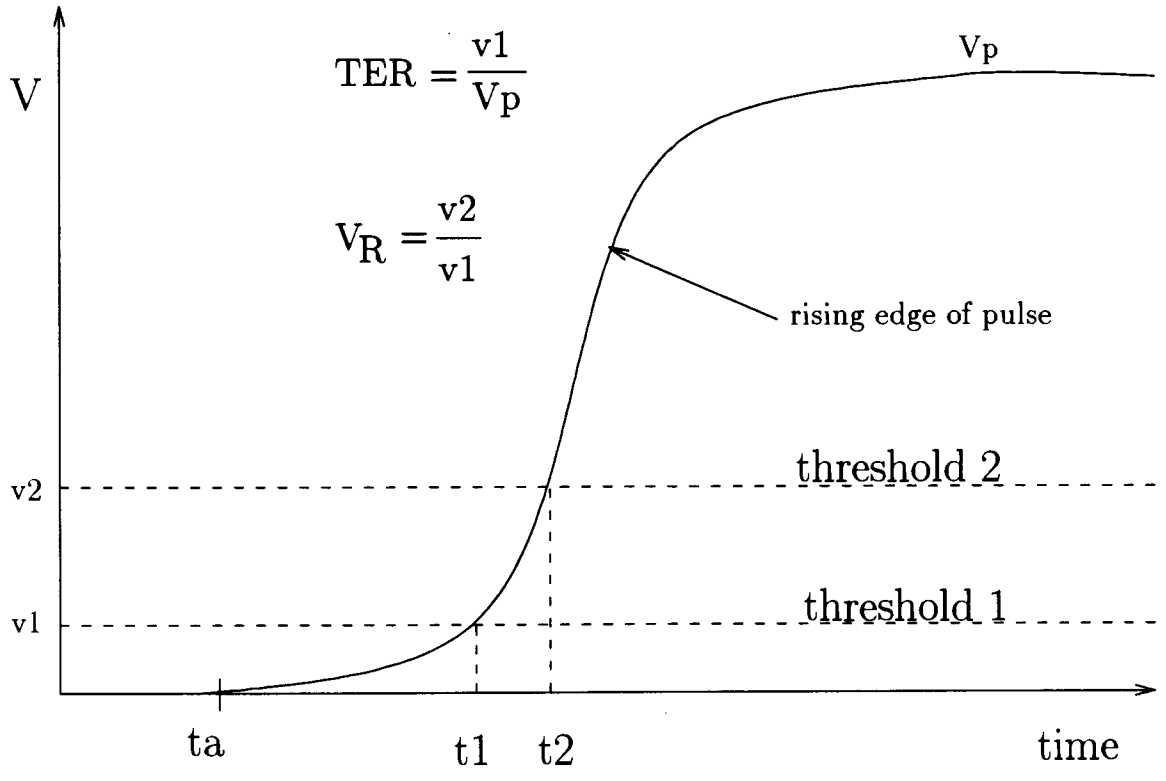

Figure 2.4: The threshold ratio $V_R \equiv \frac{v_2}{v_1}$ and the lower Threshold level to Envelope peak ratio $TER \equiv \frac{v_1}{V_p}$.

2.3 Generalized Filter Responses

Because linear systems can be defined in terms of their transfer functions, a first step in determining the order of (2.1) is to consider the characteristics of rising edges of different filter shapes.

2.3.1 First Order Low Pass Filter

The simpliest filter function, one of first order, is considered first. The transfer function is given by (Phillips and Harbor 1988)

$$F_1(s) = \frac{\alpha}{s+\alpha} \tag{2.2}$$

where $\frac{1}{\alpha}$ is the time constant of the system.

The time domain step response of the filter is

$$\begin{aligned} c_1(t) &= \mathcal{L}^{-1}\{\frac{1}{s}F_1(s)\} \\ &= [1-e^{-\alpha t}]u(t) \end{aligned} \tag{2.3}$$

where $u(t)$ is the unit step function.

Expanding the exponential in (2.3) in a Taylor series yields

$$\begin{aligned} c_1(t) &= \left\{1-\left[1-\alpha t+\frac{(\alpha t)^2}{2!}-\frac{(\alpha t)^3}{3!}+\cdots\right]\right\}u(t) \\ &= [\alpha t-\frac{1}{2}(\alpha t)^2+\cdots]u(t) \\ &\approx [\alpha t]u(t) \end{aligned} \tag{2.4}$$

where the approximation is valid for $\alpha t \ll 1$ and corresponds to the initial rising edge of the pulse.

As can be seen from (2.4), the initial rising edge of the first order low pass filter is a linear function of time.

2.3.2 General Order Low Pass Filter

It is desired to determine the lowest power of t in the expansion of the time domain step response as this will give an indication of the nature of the rising edge. The time domain step response expansion has the form

$$x(t) = a_0 + a_1 t + a_2 t^2 + \cdots + a_n t^n \tag{2.5}$$

The first non-zero coefficient encountered in (2.5) determines the lowest power of t in the expansion. The n_{th} coefficient is found by differentiating (2.5) n times and evaluating at $t = 0$ as

$$a_n = \frac{x^{(n)}(0)}{n!} \tag{2.6}$$

If the transfer function of the low pass system is known, the Laplace Initial Value Theorem and the Laplace Derivative Theorem can be used to calculate the n_{th} derivative at $t = 0$, which determines the lowest power of t and hence gives an estimate of the nature of the rising edge of the step response.

An example will show the methodology.

Given a low pass transfer function

$$F(s) = \frac{s + a}{s^3 + bs^2 + cs + d} \tag{2.7}$$

the step response is

$$X(s) = \frac{1}{s} \frac{s + a}{s^3 + bs^2 + cs + d} \tag{2.8}$$

The Initial Value Theorem combined with the Derivative Theorem, shown below

$$\lim_{t \to 0} x(t) = \lim_{s \to \infty} sX(s) \tag{2.9}$$

and

$$\lim_{t \to 0} x^{(n)}(t) = \lim_{s \to \infty} [s^{n+1} X(s) - s^n x(0) - \cdots - s x^{(n-1)}(0)] \tag{2.10}$$

is used to evaluate the coefficients in the time domain step response expansion.

Evaluating the coefficients

$$\begin{aligned} a_0 &= \lim_{t \to 0} x(t) \\ &= \lim_{s \to \infty} s \frac{1}{s} \frac{s + a}{s^3 + bs^2 + cs + d} \\ &= 0 \end{aligned}$$

and

$$\begin{aligned} a_1 &= \lim_{s \to \infty} s^2 \frac{1}{s} \frac{s + a}{s^3 + bs^2 + cs + d} \\ &= 0 \end{aligned}$$

and

$$\begin{aligned} a_2 &= \lim_{s\to\infty} s^3 \frac{1}{s}\frac{s+a}{s^3+bs^2+cs+d} \\ &= \frac{1}{2} \end{aligned}$$

Because the a_2 coefficient is the first non-zero one, the lowest power of t of the rising edge is t^2.

The leading term of the rising edge is filter dependent as the leading term in the expansion of the first order filter of the previous section was t and the leading term of the above higher order filter is t^2.

2.4 Transducer Model

Now that it has been shown that the leading term in the step response is filter dependent the equivalent circuit transducer model (Stansfield 1991) will be used to investigate the transmit receive transfer characteristics of the transducers and give a clearer idea of the shape of the rising edge of the pulse. The equivalent circuit is a conventional model for a piezo-electric sonar transducer and is shown is Figure 2.5.

The equivalent circuit models the electro-acoustic interaction in the material with a simple RLC network. Here C_o represents the electric ("static") capacitance of the transducer element, while L_m and C_m account for the inertia of the vibrating mass and its compliance respectively. The resistive terms account for losses in the material as seen from the input; R_{LOSS} represents unwanted heating losses in the material and R_{RAD} is a "radiation resistance" and accounts for the acoustic energy beamed out into the water. The voltage developed across R_{RAD} is proportional to the pressure of the outgoing acoustic wave.

This model can be used to obtain an expression for the transfer function of a sonar transducer.

2.4.1 Transmit Mode

The transfer function of the equivalent transmit model is determined by calculating the relationship between the pressure out, p_{out}, and the voltage in, V_{in}. As stated earlier, the voltage developed across the radiation resistance is proportional to the

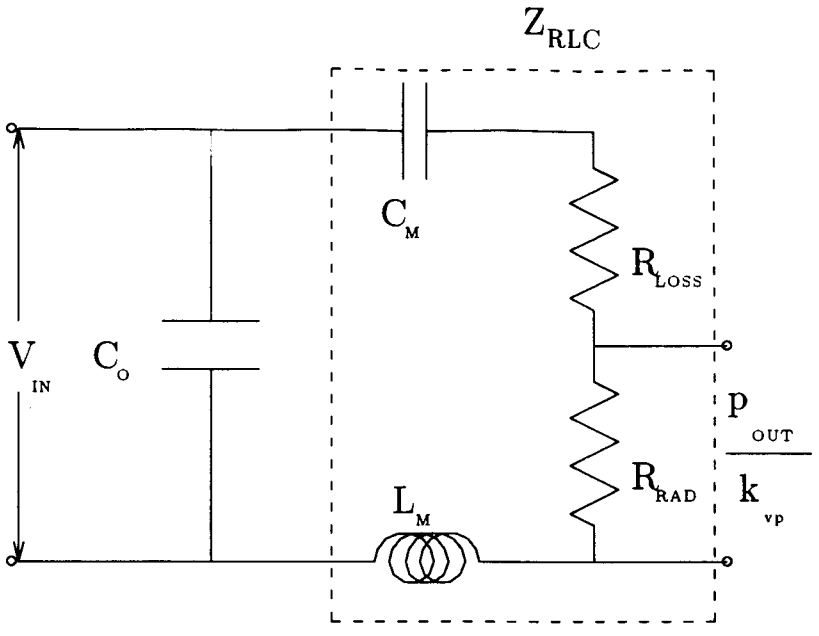

Figure 2.5: The electro-mechanical model for a piezo-electric sonar transducer acting as a projector.

pressure (i.e. $p_{out} = k_{vp} V_{RAD}$). From the above relationship and the equivalent circuit model of Figure 2.5, the ratio of the outgoing wave pressure to the applied voltage is

$$\frac{1}{k_{vp}} \frac{p_{out}}{V_{in}} = \frac{R_{RAD}}{Z_{RLC}} \tag{2.11}$$

or, from Figure 2.5,

$$\frac{p_{out}}{V_{in}} = \frac{k_{vp} \frac{R_{RAD}}{L_m} s}{s^2 + \frac{R_{LOSS}+R_{RAD}}{L_m} s + \frac{1}{C_m L_m}} \tag{2.12}$$

The transmit response is in the form of a bandpass filter. In order to project a baseband pulse, the pulse must be shifted in frequency to the resonant frequency of the transducer. This is accomplished by modulating the resonant frequency of the transducer with the baseband pulse.

2.4.2 Receive Mode

On receive, a pressure p_{in} is applied to the face of the transducer, which due to the piezo-electric nature of the ceramic generates an output voltage, V_{out}. The relationship between V_{out} and the incident pressure can be calculated from the modified transducer

model in Figure 2.6, which is applicable (Bobber 1988) when the transducer is being used as a hydrophone (receiver).

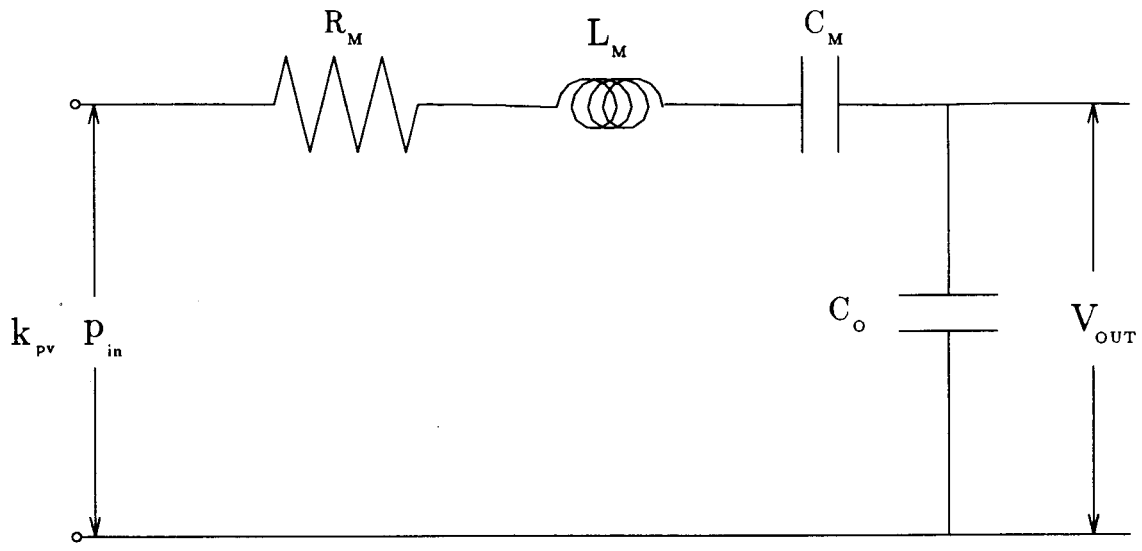

Figure 2.6: The electro-mechanical model for a piezo-electric sonar transducer acting as a hydrophone.

The resistor R_m represents the input resistance of the receiver circuit. A voltage proportional to the incident pressure is used as the input of the circuit, i.e. $V_{in} = k_{pv}p_{in}$). The ratio of output voltage V_{out} to the incident pressure is thus,

$$\frac{V_{out}}{k_{pv}p_{in}} = \frac{Z_o}{Z_o + Z_{RLC}} \tag{2.13}$$

or, from Figure 2.6,

$$\frac{V_{out}}{p_{in}} = \frac{k_{pv}\frac{1}{L_m C_o}}{s^2 + \frac{R_m}{L_m}s + \left[\frac{1}{L_m C_m} + \frac{1}{L_m C_o}\right]} \tag{2.14}$$

Equation 2.14 has the form of a second order low pass filter.

The combined transmit receive response of the transducer takes the form of a bandpass filter followed by a low pass filter. The two filters are isolated by the water hence their transfer functions can be multiplied in the Laplace domain. The transfer function of the combined response is,

$$F_{TR}(s) = \frac{k_{vp}\frac{R_{RAD}}{L_m}s}{\left(s^2 + \frac{R_{LOSS}+R_{RAD}}{L_m}s + \frac{1}{C_m L_m}\right)} \frac{k_{pv}\frac{1}{L_m C_o}}{\left(s^2 + \frac{R_m}{L_m}s + \left[\frac{1}{L_m C_m} + \frac{1}{L_m C_o}\right]\right)} \tag{2.15}$$

or

$$F_{TR}(s) = \frac{k_R \frac{R_m}{L_m} s}{\left(s^2 + \frac{R_m}{L_m} s + \frac{1}{L_m C_m}\right)} \frac{\frac{1}{L_m C_o}}{\left(s^2 + \frac{R_m}{L_m} s + \frac{1}{L_m C_m} + \frac{1}{L_m C_o}\right)} \tag{2.16}$$

where $R_m \equiv R_{RAD} + R_{LOSS}$ and $k_R = k_{vp} k_{pv} \frac{R_{RAD}}{R_{RAD}+R_{LOSS}}$

Equation 2.16 can be expressed in a more general form

$$F_{TR}(s) = k_R \frac{2\xi\omega_0 s}{(s^2 + 2\xi\omega_0 s + {\omega_0}^2)} \frac{{\omega_1}^2}{(s^2 + 2\xi\omega_0 s + {\omega_0}^2 + {\omega_1}^2)} \tag{2.17}$$

where ${\omega_0}^2 = \frac{1}{L_m C_m}$, ${\omega_1}^2 = \frac{1}{L_m C_o}$ and $\xi = \frac{R_m}{L_m} \frac{1}{2\sqrt{L_m C_m}}$.

Because the combined transmit receive response is bandpass, the Initial Value Theorem cannot be used to determine the leading term of the complex envelope in the time domain response. The Laplace domain bandpass step response was determined, $Y(s) = \mathcal{L}\{\sin\omega_0 t u(t)\} F_{TR}(s)$, and using the symbolic math package "Maple" (Waterloo Maple Software 1992), the time domain bandpass step response was found to be

$$\begin{aligned} y_{BP}(t) \;=\; & \frac{{\omega_1}^4}{4{\omega_0}^4\xi^2 + {\omega_1}^4} \sin\omega_0 t - \frac{2{\omega_1}^2\xi{\omega_0}^2}{4{\omega_0}^4\xi^2 + {\omega_1}^4} \cos\omega_0 t \\ & - \frac{1}{\beta} e^{-\xi\omega_0 t} \sin\omega_0\beta t \\ & + \frac{2\xi^2{\omega_0}^3 [2{\omega_0}^2 + {\omega_1}^2]}{(4{\omega_0}^4\xi^2 + {\omega_1}^4)\sqrt{{\omega_0}^2\beta^2 + {\omega_1}^2}} e^{-\xi\omega_0 t} \sin\sqrt{{\omega_0}^2\beta^2 + {\omega_1}^2}\, t \\ & + \frac{2{\omega_0}^2{\omega_1}^2\xi}{4{\omega_0}^4\xi^2 + {\omega_1}^4} e^{-\xi\omega_0 t} \cos\sqrt{{\omega_0}^2\beta^2 + {\omega_1}^2}\, t \end{aligned} \tag{2.18}$$

The time domain bandpass response has a complex envelope, therefore to recover the in-phase component the bandpass signal must be multiplied by $\sin\omega_0 t$ and low pass filtered and to recover the quadrature component it must be multiplied $\cos\omega_0 t$ and low pass filtered. The complex envelope is then

$$\begin{aligned} y_C(t) &= [y_{BP}(t)\sin\omega_0 t + j y_{BP}(t)\cos\omega_0 t]_{LP} \\ &= y_I(t) + j y_Q(t) \end{aligned} \tag{2.19}$$

Determining the leading term in t requires expansion of all sines, cosines and exponentials of the magnitude of the complex envelope (2.19) into their power series

form, similar to the procedure of Section 2.3.1. Unfortunately this proves to be totally impractical to be carried out analytically and determination of the shape of the rising edge was done numerically using "Maple". The two point algorithm (Section 2.2) was used to fit the normalized magnitude of the complex envelope for various values of n. The nature of the rising edge was evaluated by maintaining a constant threshold ratio, ($V_R = \frac{V_2}{V_1}$) and sliding the two threshold levels along the rising edge of the pulse. From Figure 2.7, it can be seen that a linear fit of two threshold samples gives the least error over the entire rising edge of the equivalent circuit model pulse.

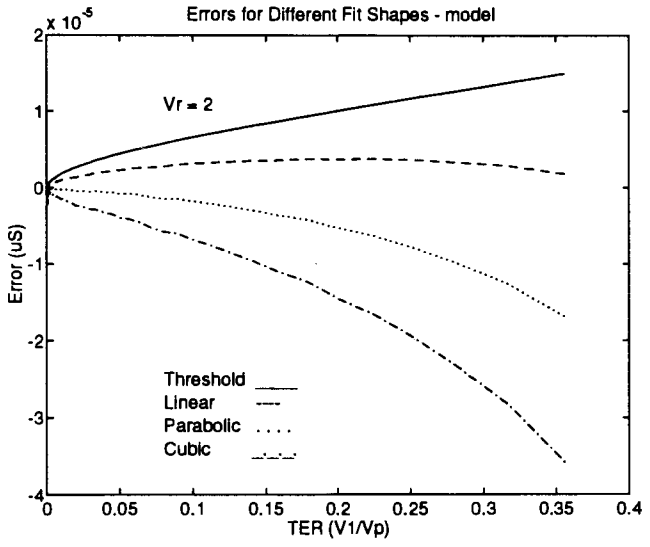

Figure 2.7: The magnitude of the equivalent circuit model complex envelope was fit with various shaped curves. The error is the difference between the actual time of arrival and the estimate. This error is calculated for the different fit shapes over various portions of the rising edge represented by the threshold settings. The ratio between the two thresholds was set at 2.

The equivalent circuit model assumes that the thickness dimension of the transducer is much smaller than any other transducer dimension. For the transducers used in this thesis, this assumption is NOT true and the model is expected to give only a first estimate of the shape.

To determine the shape of the rising edge of the specific transducers a pulse was transmitted and received with the physical transducers. The received envelope was digitized and averaged and the two point algorithm was used with various values of n to fit the rising edge of the pulse.

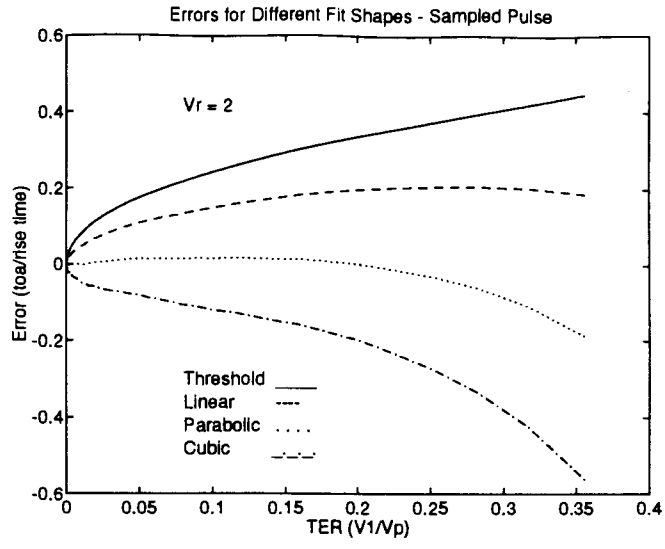

Figure 2.8: A pulse was sent through the transmit-receive pair of transducers then digitized, normalized and the rising edge was fit with various shaped curves. The error is the difference between the actual time of arrival and the estimate. This error is calculated for the different fit shapes over various portions of the rising edge represented by the threshold settings. The ratio between the two thresholds was set at 2.

As can be seen from Figure 2.8, the rising edge of the pulse of the transmit-receive waveform fits the parabolic curve with the least amount of errors over the rising edge of the pulse. The type of graph shown in Figure 2.8, Timing Error as a function of the threshold locations, will be used throughout the rest of this thesis to make comparisons of theoretical and experimental results.

It is particularly instructive to compare the difference in accuracy resulting from the parabolic fit and that obtained from the single threshold crossing method. It can be seen in Figure 2.8 that the parabolic fit provides a substantial improvement in accuracy and yet involves little or no circuit complexity or computational demands.

2.5 Threshold Level Selection

The question of how to set the two threshold levels in order to cover the widest range of probable signal levels with the least amount of error must be addressed. The error is the time difference between when the pulse actually arrives and the estimate of the

arrival time.

To determine the proper choice of threshold levels and threshold ratios, the parabolic algorithm and the uncertainties associated with it are considered as well as the parabolic nature of the rising edge for various threshold levels and ratios.

The parabolic algorithm is considered first. The parabolic time of arrival is calculated from

$$t_a = \frac{\sqrt{v_2}t_1 - \sqrt{v_1}t_2}{\sqrt{v_2} - \sqrt{v_1}} \tag{2.20}$$

The uncertainty in this calculation is affected by uncertainties in the measured quantities, v_1, v_2, t_1, t_2. Because the errors in all the measured quantities are uncorrelated the uncertainty in the time of arrival is

$$\begin{aligned} \Delta t_a &= \sqrt{\left(\frac{\partial t_a}{\partial t_1}\Delta t_1\right)^2 + \left(\frac{\partial t_a}{\partial v_1}\Delta v_1\right)^2 + \left(\frac{\partial t_a}{\partial t_2}\Delta t_2\right)^2 + \left(\frac{\partial t_a}{\partial v_2}\Delta v_2\right)^2} \\ &= \sqrt{\frac{V_R+1}{\left[\sqrt{V_R}-1\right]^2}\Delta t^2 + \frac{1}{4a}\left[V_R + \frac{1}{V_R}\right]\frac{1}{v_1\left[\sqrt{V_R}-1\right]^2}\Delta v^2} \end{aligned} \tag{2.21}$$

where $V_R \equiv \frac{v_2}{v_1}$, $\Delta v \equiv \Delta v_1 = \Delta v_2$, $\Delta t \equiv \Delta t_1 = \Delta t_2$, v_1 is the lower threshold level and a is the curvature of the parabola.

Figure 2.9 shows how the uncertainty in the time of arrival, Δt_a, behaves for various values of the lower threshold level v_1 and over a wide range of threshold ratios V_R. The curvature of the parabola, a, is set to a typical value of $0.035\frac{V}{\mu S^2}$ which was determined through experiment, $\Delta v = 10mV$ and $\Delta t = \frac{1}{2}T_{clock} = 0.25\mu S$.

It can be seen from Figure 2.9, and (4.4), that setting the lower threshold v_1 too low increases the time of arrival measurement uncertainty , in addition to the more usual problem of the increased probability of false triggering on noise spikes. According to Figure 2.9 a good choice of the threshold ratio is between 2 and 4. Below a threshold ratio of 2 the error increases sharply and above 4 there is no real benefit. The choice of v_1 has little effect if the ratio is chosen above 2.

Next the parabolic nature of the rising edge is investigated. Using the digitized pulse, V_R was fixed and the thresholds were slid over the entire rising edge to observe the parabolic nature of the curve. This was performed for various threshold ratios to examine the effects of threshold levels and threshold ratios. Figure 2.10 shows that the lower portion of the rising edge is the most parabolic as the error goes to zero.

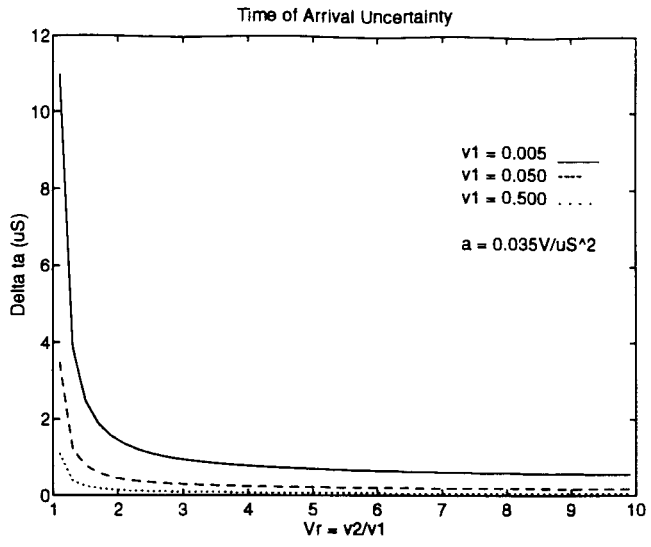

Figure 2.9: The uncertainty in the time of arrival parabolic algorithm is examined for various values of v_1 and over a wide range of V_R.

The rising edge of the pulse has three distinct portions as shown by Figure 2.11. Portion 1 is the initial part of the rising edge and has a concave up shape. Portion 2 is the central part of the rising edge and has an almost linear shape. The third part, Portion 3, is the knee of the rising edge and has a concave down shape. Figure 2.11 will prove useful in describing the shape of the error curves shown in Figure 2.10.

In the lower portion of the rising edge, Portion 1, the t^2 term dominates and the parabolic fit works well resulting in small errors. As the thresholds are slid up the rising edge, from portion 1 to portion 2, the t^2 term ceases to dominate; the higher order powers of t become more significant, the parabolic assumption begins to waver and the curve begins to rise more sharply. In order to compensate for the sharper rise the curvature parameter of the parabola must be increased and as a result the predicted start of the pulse is after the actual start of the pulse. This phenomena is shown in Figure 2.10 as the error gradually becomes more positive.

Continuing up the rising edge the curve begins to flatten in portion 3 and again the parabolic assumption loses validity. Due to the flatness, the parabolic curvature needs to be reduced to fit the two threshold samples with a parabola and the fitting algorithm predicts the start of the pulse before it actually arrives. The prediction turns sharply negative as the upper threshold nears the pulse peak where the curve

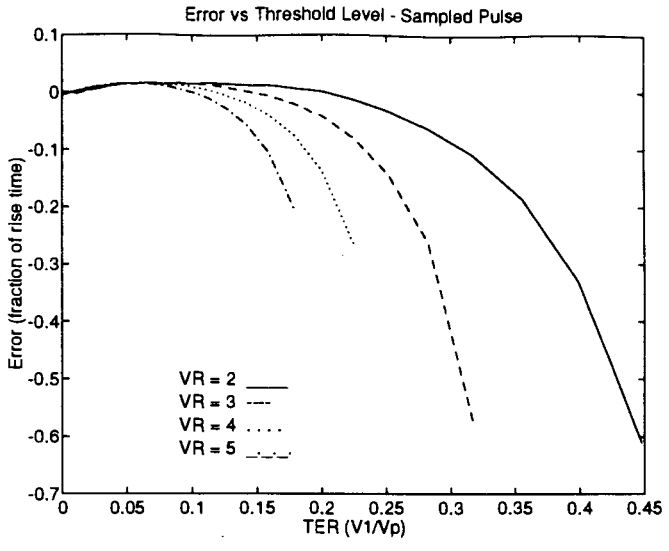

Figure 2.10: The digitized pulse was used to simulate the two point parabolic fit time-of-arrival estimator. The error is the difference between the actual time of arrival and the estimate. This error is determined as a function of the threshold locations represented by the ratio between the lower threshold v_1 and the peak envelope level V_p. $TER = \frac{v_1}{V_p}$

is the flattest.

From Figure 2.10 it can be seen that the lower v_1 the better the parabolic assumption and the smaller V_R the higher v_1 can be slid up the rising edge before the estimate is over run with errors. Figures 2.9 and 2.10 seem to contradict one another. A compromise must be reached between threshold levels and threshold ratios.

The threshold ratio should be set as small as possible to take advantage of the increases in useful rising edge area where the parabolic assumption can be used, but high enough that the large errors in the time of arrival uncertainty are not prevelant. Therefore the ratio should be set in the $V_R = 2$ to 4 region.

Since the parabolic assumption is most valid on the lower portion of the rising edge and v_1 has minimal effects on the time of arrival uncertainty, the lower threshold should be set based on the noise level. The signal plus noise distribution at the output of the envelope detector is Rician as will be shown later. For small signal levels the Rician distribution approaches that of a Rayleigh distribution (Middleton 1987). To obtain a probability of false alarm of P_{false} given Rayleigh distributed noise, the threshold should be set to

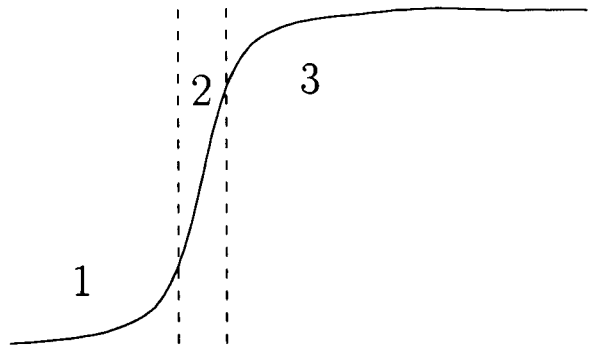

Figure 2.11: The rising edge of the pulse has three distinct portions: lower portion - concave up, central portion - almost linear, and knee portion - concave down.

$$P_{false} = e^{-\frac{v_1^2}{2\sigma^2}} \tag{2.22}$$

and solving for v_1

$$v_1 = \sqrt{2 \ln \left[\frac{1}{P_{false}} \right]} \sigma \tag{2.23}$$

where σ is the variance of the noise.

2.6 Noise

The accuracy of the time of arrival estimate depends largely on the noise in the system. If the noise is small then the SNR will be large and the two samples will be in the parabolic range even when the signal levels are lower. The sources of noise must be identified, characterized and then analyzed to determine their effects on the system.

The sources of noise on the system can be classified into three categories:

1. Ambient Acoustic Noise
2. Electronic Noise
3. Quantization Noise

2.6.1 Ambient Acoustic Noise

The sources of ambient noise are both natural and man-made. Natural sources include seismic disturbances, agitation of the surface by wind (wind noise), thermal activity of the water molecules (thermal noise) as well as the sounds generated by aquatic mammals and fishes. Distant ships are the dominant source of man-made ambient noise in the oceans.

Ambient noise is usually considered in three acoustic spectrum bands. The low frequency band, 1Hz to several hundred Hertz, is dominated by distant shipping. In the mid-frequency band, several hundred Hertz to around 50kHz, wind noise is the principal contributor and in the high frequency band, above 50kHz, thermal noise effects dominate (Urick 1983).

The URL system uses transducers operating at a resonant frequency of 125kHz, which is well into the high frequency range discussed above and thus the dominant source of ambient acoustic noise is thermal.

The acoustic noise level generated by high frequency thermal noise can be represented by (Urick 1983)

$$N_{thermal} = -75 + 20log_{10}f + 10log_{10}BW \tag{2.24}$$

where f is the frequency, in kHz, BW is the equivalent noise bandwidth of the system and $N_{thermal}$ is in dB.

The noise level can also be expressed as

$$N_{thermal} = 10log_{10}\frac{I_{NT}}{I_{ref}} \tag{2.25}$$

where I_{NT} is the noise intensity and $I_{ref} = \frac{p^2}{\rho c}$ is the intensity which results from a plane wave of rms pressure of $1\mu Pa$ in water (ρ is the density of water and c is the speed of sound in water) .

Equating (2.24) and (2.25)

$$I_{NT} = 666.7\left(10^{-28.5}\right)f^2BW \tag{2.26}$$

where $\rho = 1000\frac{kg}{m^3}, c = 1500\frac{m}{s}$.

The acoustic noise received depends on the bandwidth of the transducer and therefore will be evaluated in Section 3.1 when the transducer specific information is discussed.

2.6.2 Electronic Noise

There are three sources of electronic noise (Analog Devices Inc. 1992):

1. Voltage Noise of the Op-Amp - The op-amp noise voltage appears in series with the two input terminals of the op-amp and is subsequently amplified.

2. Current Noise of the Op-Amp - The op-amp current noise appears at the input terminals of the op-amp and is important if it flows through an impedance to produce a voltage which the op-amp then amplifies.

3. Johnson or Thermal Noise of the resistors in the circuit - All resistances, but not reactive impedances, generate a noise voltage which is equal to $\sqrt{4kTBR}$ where k is Boltzmann's constant , T is the absolute temperature in $^{\circ}K$, B is the bandwidth and R is the resistance.

Figure 2.12 illustrates the effect of all three electronic noise sources on an amplifier circuit.

For a standard inverting configuration, appropriate for the pre-amp used in this system, there are six sources of uncorrelated noise. Each one will be considered separately.

1. Thermal Noise in resistor R_3 : The thermal noise e_3 generated from R_3 appearing at the output of the amplifier is

$$v_1 = \frac{(R_1 + R_2)}{R_1}\sqrt{4kTBR_3} \tag{2.27}$$

2. Thermal Noise in resistor R_1 : The thermal noise e_1 generated from R_1 appearing at the output of the amplifier is

$$v_2 = -\frac{R_2}{R_1}\sqrt{4kTBR_1} \tag{2.28}$$

3. Thermal Noise in resistor R_2. The noise voltage e_2 generated from R_2 is not amplified, but buffered directly to the output. Therefore the noise voltage is

$$v_3 = \sqrt{4kTBR_2} \tag{2.29}$$

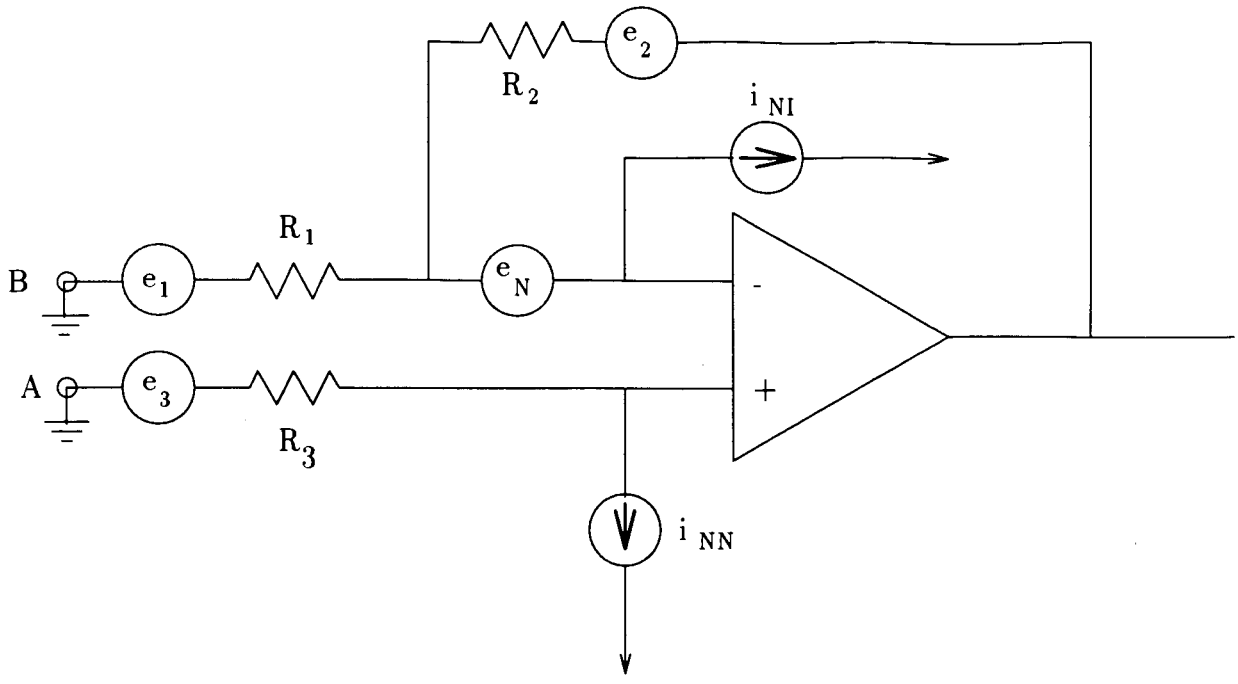

Figure 2.12: An inverting amplifier with the three source of electronic noise shown: voltage noise of the op-amp e_N, current noise of the op-amp non-inverting and inverting respectively, i_{NN} and i_{NI}, and the thermal noise of the resistors e_1, e_2 and e_3.

4. The amplifier noise voltage e_N appears at the input of the amplifier. Because of the virtual short circuit between the inverting and non-inverting inputs, it has the same effect as being applied to the non-inverting terminal. The noise voltage generated at the output of the amplifier is

$$v_4 = \frac{(R_1 + R_2)e_N}{R_1} \tag{2.30}$$

5. The noise current of the non-inverting input flows through R_3 and generates a noise voltage at the non-inverting input. This source is amplified by the non-inverting gain and is

$$v_5 = \frac{R_1 + R_2}{R_1} I_{NN} R_3 \tag{2.31}$$

6. The inverting noise current flows through the parallel combination of R_1 and R_2 and generates a noise voltage at the input to the amplifier and the result is

$$v_6 = \frac{R_1 + R_2}{R_1} \frac{I_{NI} R_1 R_2}{R_1 + R_2}$$

$$= R_2 I_{NI} \tag{2.32}$$

The root mean squared noise voltage, e_{noise}, for the six uncorrelated noise voltages, referred to the input of terminal B, is given by

$$e_{noise} = \frac{R_1}{R_2}\sqrt{{v_1}^2 + {v_2}^2 + {v_3}^2 + {v_4}^2 + {v_5}^2 + {v_6}^2} \tag{2.33}$$

The noise in the receiver section consists of the acoustic noise and the electronic noise. As will be shown later in Section 3.4 electronic noise dominates at the input of the receiver.

2.6.3 Receiver Noise Distribution

The noise in the receiver section takes on different distributions as it progresses through the system. The distribution of the noise will be examined as the signal moves through various stages of the receiver section, shown in Figure 2.13.

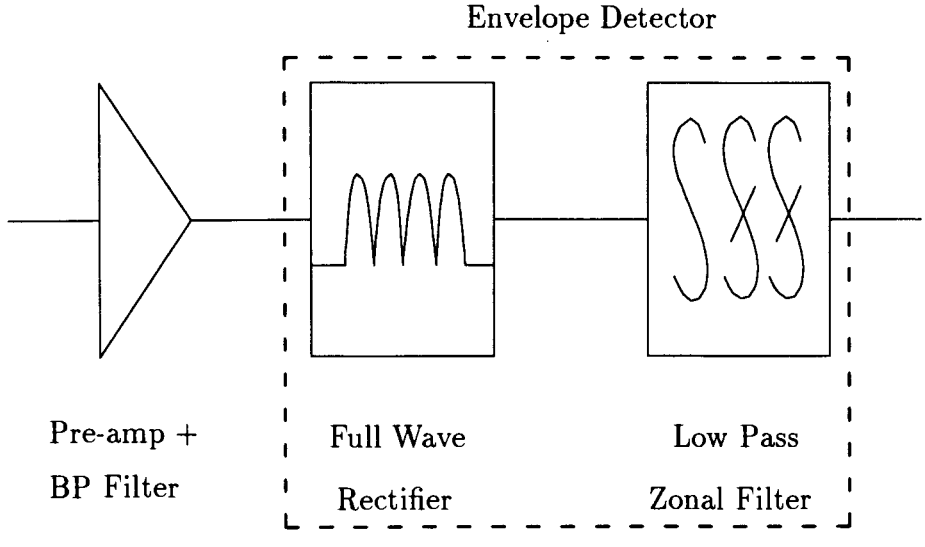

Figure 2.13: A block diagram of the receiver section. It consists of the pre-amp, the full-wave rectifier and the low pass zoning filter.

The noise referred to the input of the receiver section is dominated by electronic noise which has a zero mean Gaussian distribution (Analog Devices Inc. 1992).

The pre-amp section amplifies and bandpass filters the noise to limit the noise bandwidth and will not effect the noise distribution, thus the noise remains Gaussian

distributed. The noise is then passed through an envelope detector consisting of a full wave rectifier and a low pass zonal filter. For a zero mean Gaussian input, the output of an ideal envelope detector is Rayleigh distributed (Van Trees 1971; Papoulis 1984). In an ideal envelope detector, the full wave rectifier only takes the absolute value of the incoming signal. In this system, the full wave rectifier consists of diodes. The non-linearity of the diodes blocks the incoming signal until it reaches the turn on voltage of the diodes. In the absence of signal, the noise generated in the pre-amp circuit is blocked and the Gaussian noise at the output of the envelope detector is a result of the electronics after and including the rectifier. With the signal present, the pre-amp electronic noise will be riding atop the signal. As the signal level increases past the turn on voltage of the diodes the noise distribution at the output of the envelope detector will be Rician distributed.

Therefore, when no signal is present the noise at the output of the real envelope detector is Gaussian distributed and when the signal is present the signal plus noise is Rician distributed.

2.6.4 Quantization Noise

Quantization noise rears its ugly head during the sampling or thresholding process. The incoming signal is analog and continuous. The voltage at which the threshold is set is also analog. A digital clock is used to measure the time when the threshold is crossed. Quantization effects are in the time measurement. The incoming signal arrived some time after the clock turned to t_n and before it reached t_{n+1}. This quantization noise is uniform over the clock period.

$$Q_n = U(0, T_c) \tag{2.34}$$

Chapter 3

HARDWARE DESCRIPTION

The AUV positioning hardware was designed and built as a vital component of the whole AUV project. It consists of four multiplexed transmit channels and four independent receive channels as well as the digital logic to control them. The time of arrival system discussed in this thesis is implemented on all channels with special Time of Arrival software.

The hardware consists of six basic components: transducers, transmit/receive (T/R) switch, transmitter, receiver, transmit control logic and receiver timing contained in a XILINX 3090 field programmable gate array, and the personal computer PC which are shown in the block diagram Figure 3.1.

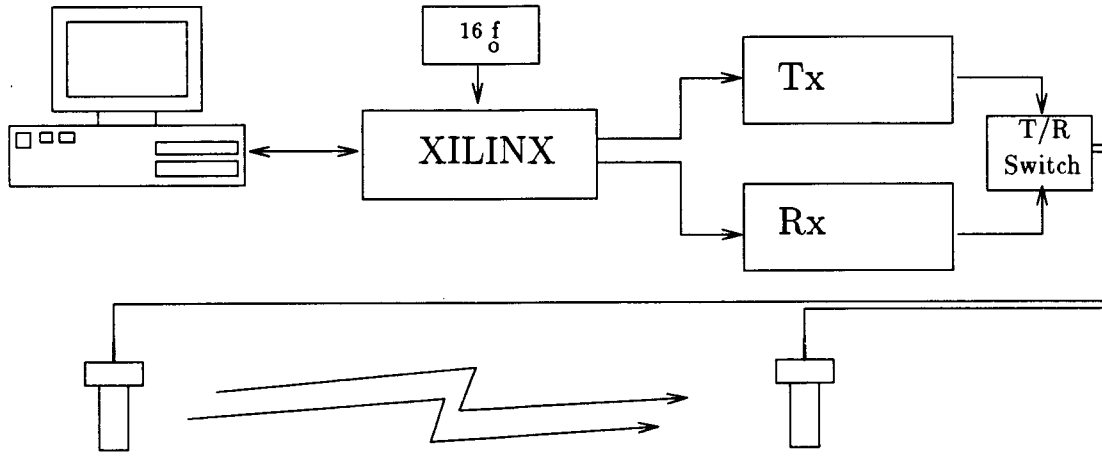

Figure 3.1: The hardware consists of six basic components:PC, XILINX, transmitter, T/R switch, receiver and the transducers.

3.1 Transducers

The transducers are PZT-4 tubular radiators having the following dimensions in meters

$$\begin{aligned} l &= 0.024 \\ r_1 &= 0.003175 \\ r_2 &= 0.00635 \end{aligned}$$

where l , r_1 and r_2 are the length, inside radius and outside radius as shown in Figure 3.2.

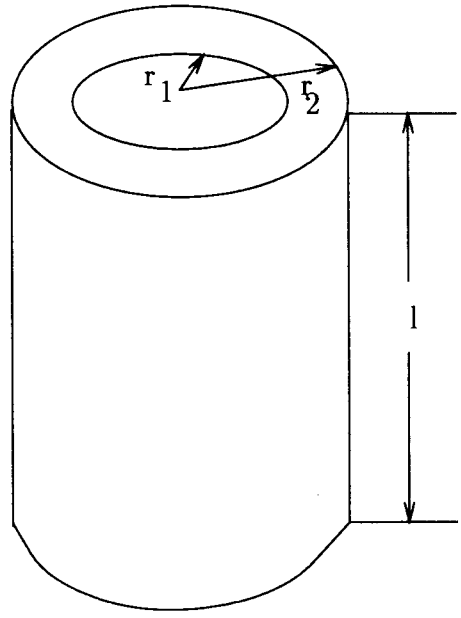

Figure 3.2: The transducers are PZT-4 tubular radiators with length = 0.024m, inside radius r_1 = 0.003175m and outside radius r_2 = 0.00635m.

The thickness dimension of the transducer gives it a nominal resonant frequency of 125kHz.

The choice of transducer frequency was made as a compromise between the high resolution of high frequency systems and long range of low frequency systems.

High resonant frequency transducers can accommodate shorter pulse lengths and

therefore have shorter rise times than lower frequency systems due to the wider bandwidth of the transducers. The chances of receiving a clean rising edge are greater at higher frequencies due to the short rise times, but because the attenuation coefficient of an underwater signal varies as f^2 (Urick 1983), the power required to obtain a given range is substantially increased as the frequency of signal is increased. For an AUV, power constraints limit the viable transducer output and long ranges cannot be obtained using frequencies greater than 1MHz. At lower frequencies the longer pulse lengths and the decreased attenuation will result in more multipath and chances of the longer rising edge remaining uncorrupt are decreased. A compromise must be made between the high power, short rise times of high frequency pulses and low power, long rise time low frequency pulses. Since it is intended to develop an Obstacle Avoidance Sonar (OAS) and side scan sonar, as well, consideration had to be taken in choosing the frequency of the positioning transducers such that there was no interference with the side scan or OAS. To avoid false positioning as a result of harmonics generated by the side scan or obstacle avoidance sonars it was decided that the frequency of the positioning sonar should be below that of the others. The side scan and obstacle avoidance sonars would be operating at frequencies above 300kHz so the positioning transducers were chosen to be 125kHz.

For use in a positioning system, the transducers should ideally be omni-directional. Omni-directionality allows the pressure wave to be radiated in all directions and received in all directions. The tubular transducers are NOT omni-directional, but because they are circular in the horizontal plane they radiate in all 360° in the horizontal plane as seen from the horizontal beam pattern shown in Figure 3.3.

The beam pattern is not truly omni-directional in the horizontal plane, as can be seen from Figure 3.3, but the transducer radiates sufficiently in all directions. The horizontal beam patterns of all the transducers used for the positioning system were measured and the one shown in Figure 3.3 is typical.

The length dimension of the transducer determines the beamwidth in the vertical plane nominally as (Urick 1983)

$$beamwidth = \frac{\lambda}{l} \tag{3.1}$$

where λ is the wavelength of the pressure wave in water and l is the length of the

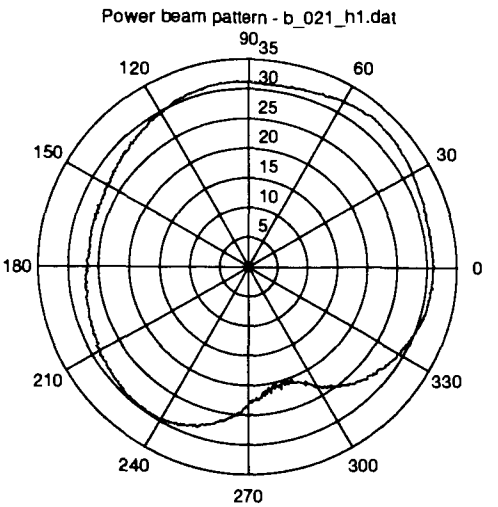

Figure 3.3: The horizontal beam pattern for a 125kHz tubular radiator used in this thesis.

transducer. The heuristically predicted beamwidth of the transducer is $\sim 28°$. The actual vertical beamwidth of the 125kHz transducer is 25-30° at zero degrees, which corresponds to the side of the transducer, as shown in Figure 3.4.

Again, the vertical beam patterns of all the transducers used for the positioning system were measured and the one shown in Figure 3.4 is typical.

The directivity index is a measure of the sharpness of the major lobe of the beam pattern. The directivity index of the transducers was found to be approximately 6.55dB using the measured beam patterns.

The bandpass frequency response (i.e. center frequency and signal bandwidth) of the transmit/receive pair of transducers is used in determining the frequency response characteristics of the filters in the receiver. Therefore it is necessary to obtain experimentally the bandpass frequency response of the transducers in a transmit/receive pair. A pulse of a given frequency was transmitted from a transducer, reflected off the surface of the water, a nearly perfect reflector (Urick 1983), then received on the same transducer. The frequency of the pulse was varied around the transducer resonance to determine the transducer frequency characteristics. Figure 3.5 shows the transmit receive frequency response of that transducer.

The -3dB bandwidth can be seen to be 10kHz with a center frequency of 128kHz.

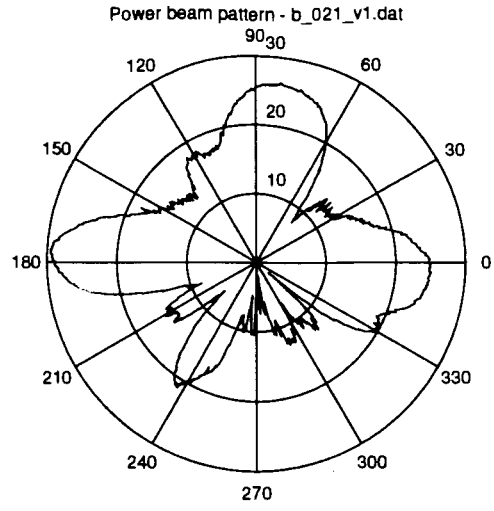

Figure 3.4: The vertical beam pattern for a 125kHz tubular radiator used in this thesis.

The acoustic noise received by the transducer depends on the bandwidth, the directivity index and the efficiency of the transducers. The efficiency of the transducers was approximated as 0.3 and the acoustic noise was found to be $/tilde 0.007 \mu V_{rms}$ at the input to the pre-amp using equation (2.26) of section 2.6.1.

The system is most efficient when the transducers are driven at their resonant frequency. Therefore the transmitter should generate a high voltage signal at this frequency.

3.2 T/R Switch

The transmit/receive switch is used to protect the sensitive pre-amp of the receiver from the high voltage pulses when the system is transmitting and to isolate the receiver from the transmitter when the system is receiving acoustic signals. Figure 3.6 shows the schematic for the transmit/receive switch.

Diodes D_1 and D_2 are used to isolate the transmitter from the receiver when the transducer is receiving a signal, since every realistic signal is too small $<\sim \pm 0.7v$ to turn on either of these diodes while at the same time allowing the high voltage transmit

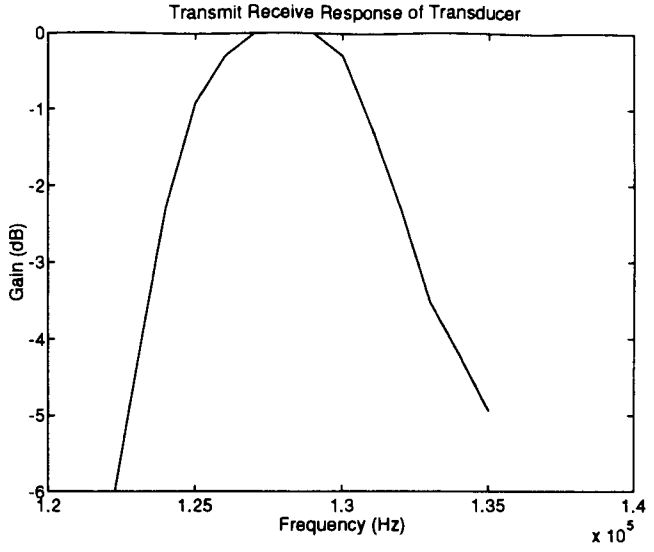

Figure 3.5: The combined transmit/receive frequency response as determined by bouncing a pulse off the surface of the water.

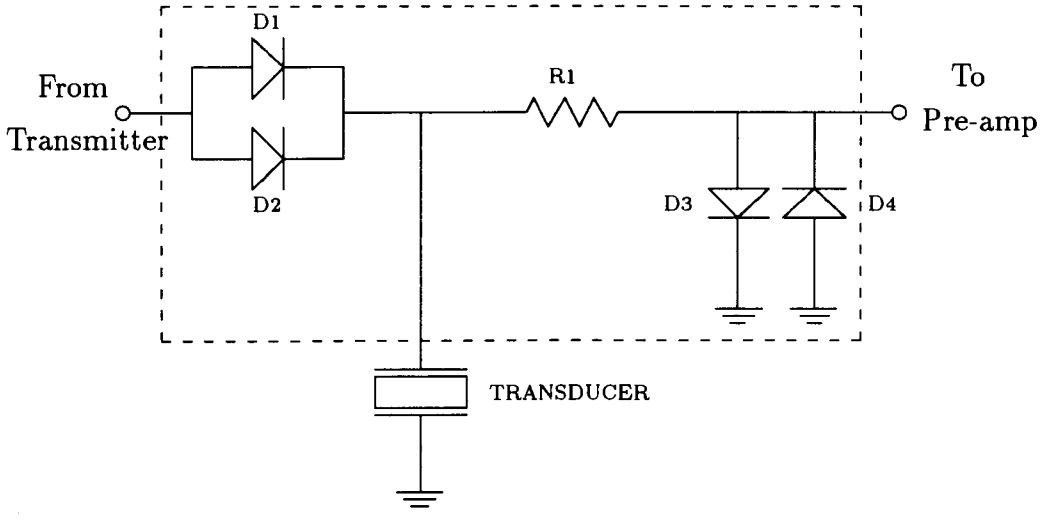

Figure 3.6: The transmit/receive T/R Switch.

pulse to pass through undisturbed. Diodes D_3 and D_4 are used to protect the pre-amplifier by clipping any transmit leakage pulse to $\sim \pm 0.7v$. Because these diodes are basically shorts to ground, the resistor R_1 is inserted so that some current flows through the transducer and acoustical power is projected into the water. The larger R_1 the more current flows through the transducer and the more power is projected into the water. On receive R_1 acts as a voltage divider and reduces the incoming signal into the pre-amp. The smaller R_1 the larger the incoming signal into the pre-amp. A compromise must be made in choosing the value of R_1. On transmit, the current through the transducer is given by

$$I_{xducer} = \frac{R_1}{R_{xducer} + R_1} \tag{3.2}$$

where R_{xducer} is the transducer impedance
and on receive the voltage into the pre-amp is given by

$$V_{pre-amp} = \frac{R_{pre-amp}}{R_{pre-amp} + R_1} \tag{3.3}$$

where $R_{pre-amp}$ is the pre-amp input impedance
and the combined response is

$$Combined = \frac{R_1}{R_{xducer} + R_1} \frac{R_{pre-amp}}{R_{pre-amp} + R_1} \tag{3.4}$$

To maximize the combined response, (3.4) is differentiated and set to zero resulting in

$$R_1 = \sqrt{R_{xducer} R_{pre-amp}} \tag{3.5}$$

For the 125kHz transducers used in this thesis, the transducer impedance is approximately 500Ω and the pre-amp input impedance for the pre-amp configuration used in the receive is approximately 1kΩ. Therefore, the best choice of R_1 is approximately 700Ω. For convenience a 680Ω resistor was chosen.

3.3 Transmitter

The transmitter, shown in Figure 3.7, is primarily composed of MOS-FET transistors acting as switches. Because not more than one transducer will be required to transmit

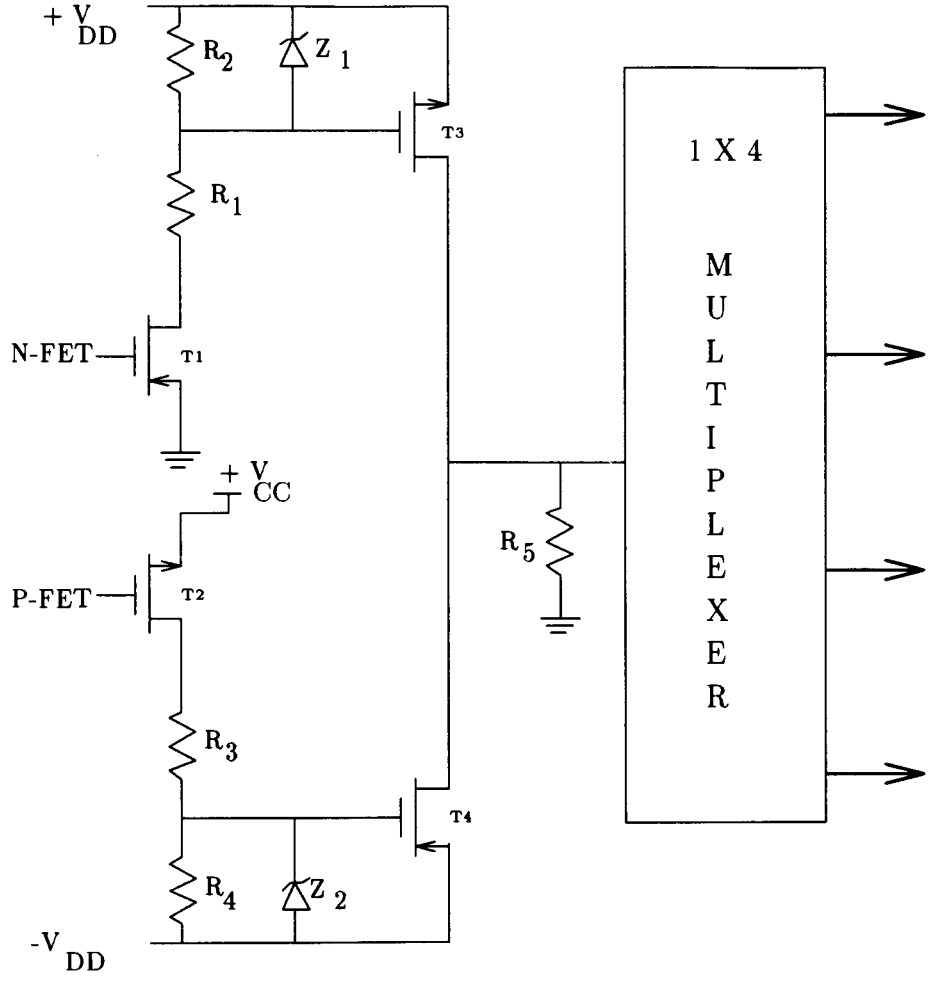

Figure 3.7: The transmitter with control signals N-FET and P-FET generated by the XILINX chip.

at one time there is only one transmitter circuit. The high voltage transmit signal is multiplexed to any of the four transducers via a set of relays.

The transmitter needs to generate a high voltage signal at the resonant frequency of the transducers. It would be more efficient to transmit a gated sine wave, where 100% of the power would be transmitted at the fundamental, f_o, as opposed to about 80% for a square wave, but the loss of efficiency was compromised to reduce the circuit complexity.

In order for the transmitter circuit as shown to generate the required high voltage signal the transmitter control signals must also be at the resonant frequency of the transducers and be as shown in Figure 3.8, where the control signal N-FET goes to the input of the N channel MOS-FET transistor T_1 and the control signal P-FET goes to the P channel MOS-FET transistor T_2.

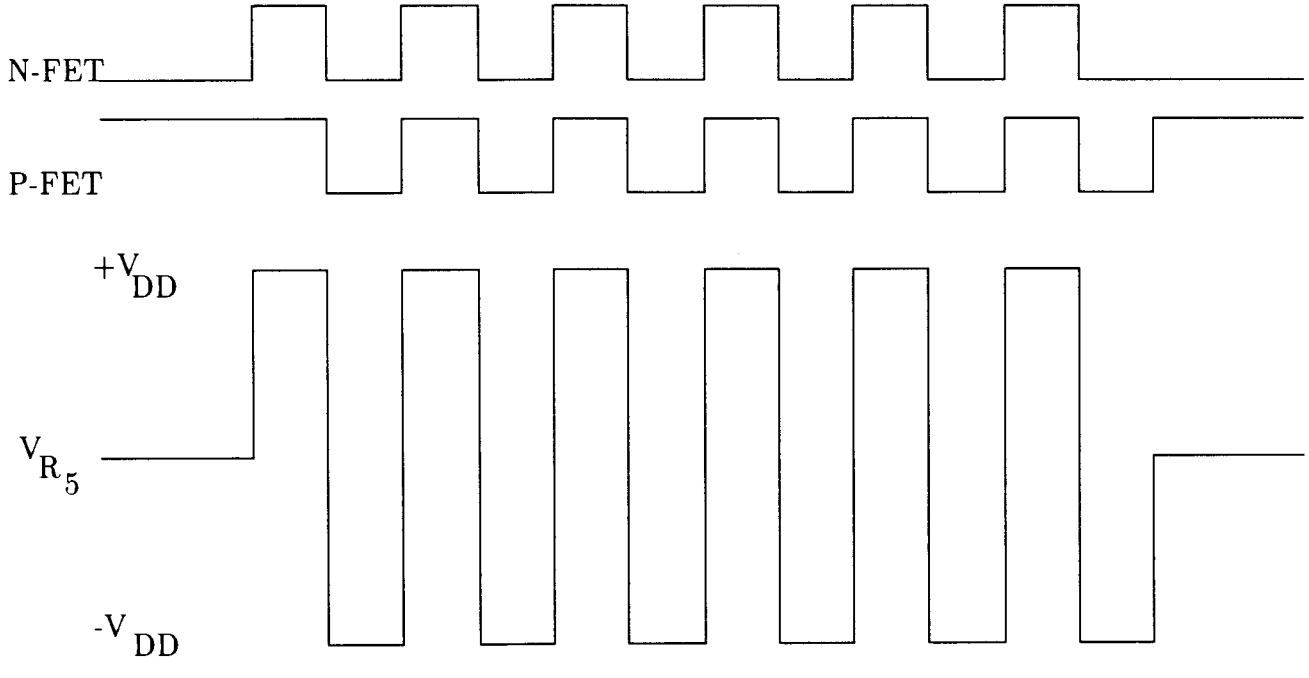

Figure 3.8: The transmit control signals, N-FET and P-FET and the resultant output transmit waveform.

When control signal N-FET is high transistors T_1 and T_3 turn on and the voltage $+V_{DD}$ appears across resistor R_5. When N-FET is low T_1 and T_3 are off. When control signal P-FET is low transistors T_2 and T_4 turn on and the voltage $-V_{DD}$ appears across resistor R_5. When N-FET is high T_1 and T_3 are off. In this manner

the high voltage gated square wave pulse is generated at the resonant frequency of the transducer and when no pulse is to be transmitted all the transistors are off and the output voltage is zero. Resistor R_5 is there as a load in case the transducer is not connected.

Resistors R_1, R_2 are used as a voltage divider so that when transistor T_1 is on the voltage at the gate of transistor T_3 is lower than its source voltage and transistor T_3 also turns on. The zener diode Z_1 is there to limit the voltage between the gate and source of transistor T_3 as excessive voltage differences between the gate and source could damage the transistor.

Resistors R_3 and R_4 and the zener Z_2 are the counterparts to R_1, R_2 and Z_1 and serve the same function for transistor T_4.

The relays are switched by the PC through the logic on the XILINX chip. The high voltage transmit voltage can then be multiplexed to whichever transducer is desired.

3.4 Receiver

Figure 3.9 shows the block diagram for the receiver.

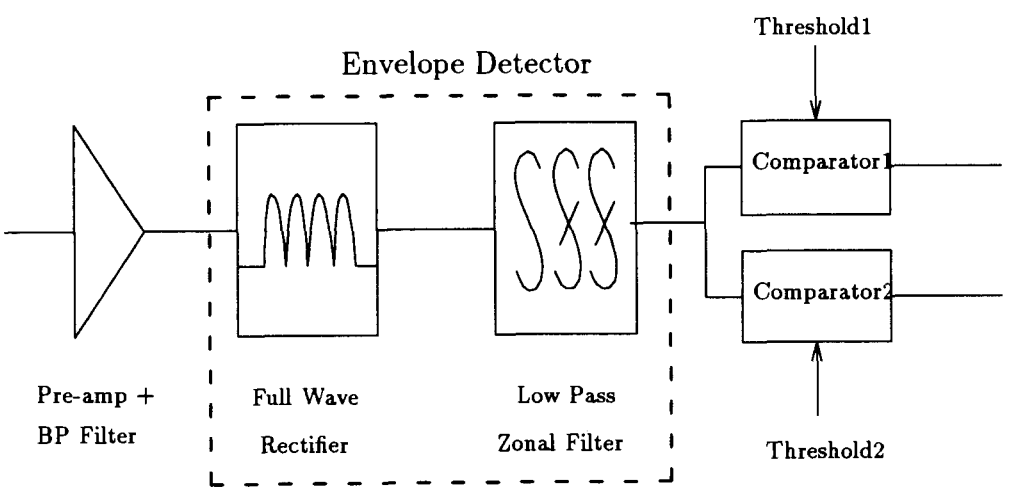

Figure 3.9: The receiver block diagram.

There are three distinct components to the receiver: the pre-amp, the envelope recovery and the threshold detection sections.

The pre-amplifier section consists of a low noise amplifier, Linear Technologies LT1028 - Ultra Low Noise Op-amp, and a 70kHz bandwidth bandpass filter centered at the resonant frequency of the transducers. The main purpose of the filter is to reduce the amount of noise that is amplified. The filter bandwidth must be chosen narrow enough to reduce the noise and wide enough so as to not affect the shape of the envelope of the incoming signal. The transducer resonant frequencies are not all the same and vary around 125kHz by $\pm$ 5kHz. The filter should be wide enough to accommodate this variation in center frequencies. A 70kHz bandwidth was chosen to account for all these factors. Care must be taken when choosing the amplifier. Amplifiers with small noise voltages and currents should be chosen since most of the receiver noise is generated at this stage.

Using the the electronic noise theory of Section 2.6.2, the rms receive noise, referred to the input of the pre-amp, is $1.2\mu V_{rms}$. Comparing the electronic noise to the acoustic noise of $\sim 0.007\mu V_{rms}$ it can be seen that the predominant source of noise of the receiver is the electronic noise generated by the pre-amplifier circuit.

The envelope of the received signal is recovered by full wave rectifying the incoming signal then passing it through a third order low pass zonal filter with a cut-off frequency of 60kHz. The low pass filter must be wide enough not to effect the shape of the envelope and narrow enough to eliminate any ripple caused from the double frequency component generated by the full wave rectifier. Two threshold levels are set using precision potentiometers, one for each comparator, for use in the two point parabolic fit. When the signal exceeds each of the preset levels a TTL rising edge is generated by the comparator and sent to the counter circuitry in the XILINX chip to disable the counters.

3.5 XILINX

The XILINX 3090 is an 80 pin field programmable gate array that contains the circuit which handles the PC interface (I/F) circuitry, such as address decoding logic and bus transceiver logic, as well as generating the transmit control signals, operating the delay timing counters and generating the hardware interrupt signifying that data is available. The XILINX circuitry requires a digital clock input for use with the receive counters and the transmit pulse generation. The frequency of the clock was

chosen to be sixteen times the resonant frequency of the transducers. This $16f_o$ clock signal is used for the receive counters and is also conveniently divided down to f_o, the resonant frequency of the transducers, for use in the transmit pulse generation. Figure 3.10 shows a block diagram of the internal logic of the XILINX gate array. There is only one transmit circuit, the output of which is multiplexed onto the four transmit channels via relays. Therefore only one channel can transmit at one time, but all channels can receive simultaneously.

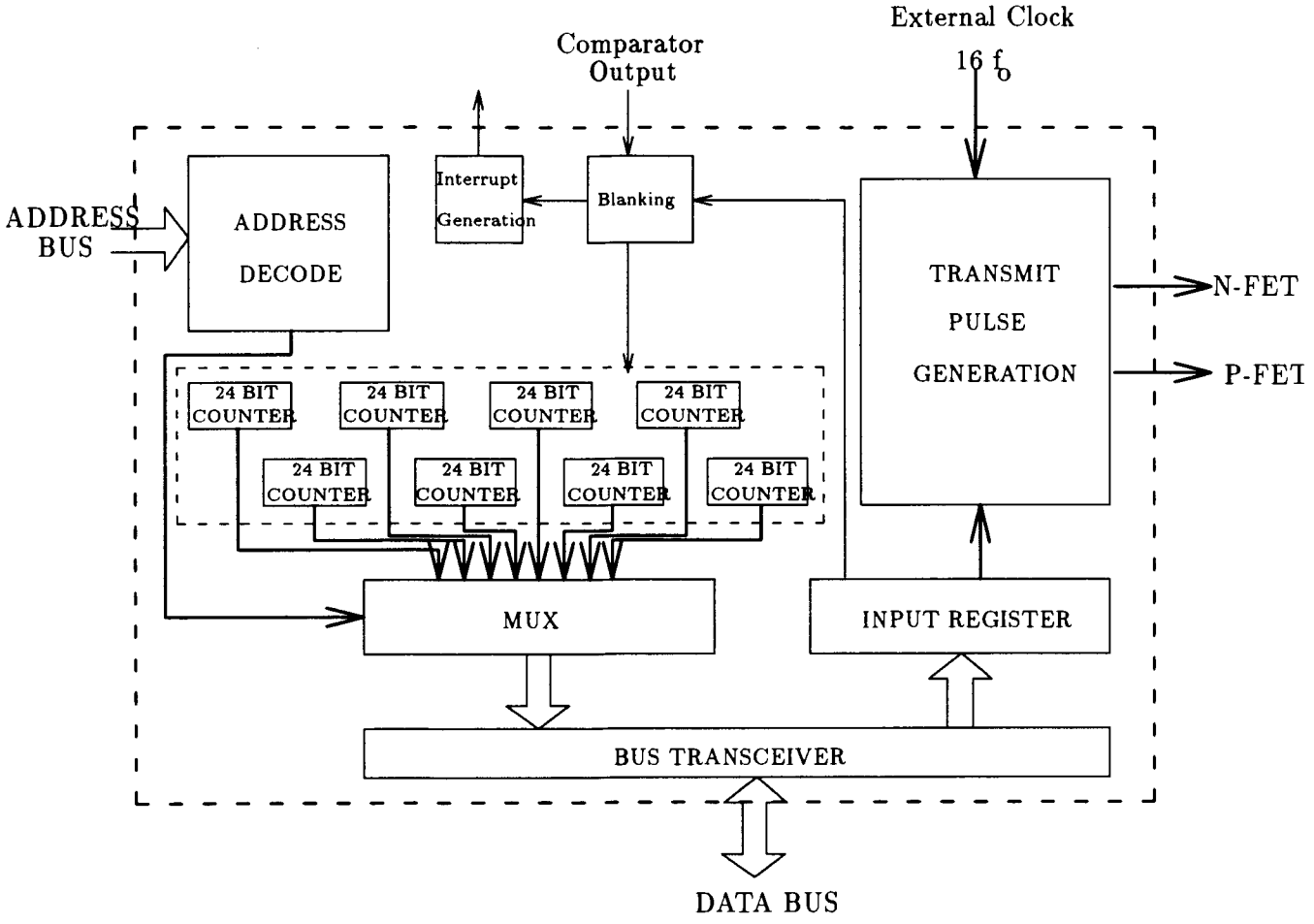

Figure 3.10: The internal block diagram of the XILINX gate array.

The PC software can be used to setup the XILINX on the fly. For instance, the receive channels can be enabled or disabled as required. The transmit and blanking times can be altered as well as the channel on which transmission occurs.

The transmit control signals generated by the XILINX, N-FET and P-FET, are

done such that the start of the transmit pulse and the start of the receive counters are synchronized to the rising edge of a carrier cycle,f_o. In this way the length, in carrier cycles, of the transmit pulse can be controlled and the start of the counters are synchronized to the start of transmission. This reduces the timing error as there will only be uncertainty as to when the pulse was received not when it was transmitted.

On receive, the threshold detector circuits generate a rising edge when the threshold is exceeded. This rising edge is used to deactivate the 24 bit receive counter associated with that threshold. When all enabled thresholds are crossed a hardware interrupt is generated informing the PC that the count data is available.

3.6 PC

A PC is used to control the all the AUV tasks, such as motor control, navigation, positioning, and imaging. The real time kernel links the AUV positioning system and the other AUV systems. The toa software, however, is written as a stand alone program on a dedicated PC. The toa software both initiates and terminates the toa estimation process.

To initiate the toa process the software must initialize the XILINX, preselect the transmit and receive channels, set the transmit pulse length and set the receiver blanking time. The blanking deactivates the receiver for a specified time after transmit so that a false trigger is not generated in the event that the transducer continues ringing after the transmit pulse. The software that runs on the PC operates in a simple loop that continuously tells the XILINX to transmit a pulse. The two point parabolic fit is performed as required in the hardware interrupt handler. No other functions are required to test the toa system.

When the receive pulse crosses the preset thresholds a hardware interrupt is generated by the XILINX which informs the PC that a receive pulse has been received and the timing information is available to be read from the XILINX. This timing information is in the form of a 24 bit counter value representing the number of clock periods, $\frac{1}{16f_0}$ that have elapsed since transmit. The two point parabolic fit algorithm is applied using these times and pre-programmed threshold levels to calculate the time of arrival estimate.

Chapter 4

EXPERIMENTAL RESULTS

A series of experiments were devised in order to characterize the factors affecting the timing accuracy of the toa system. These factors include any constant system bias and any non-constant effects associated with the parabolic approximation and the SNR levels. These factors were then used to evaluate the quality of the time of arrival estimate.

The time of arrival system measures the time it takes for a pressure wave to travel from one transducer to another. In order to verify the time of flight measurement the actual time of travel must be known. However, only the physical distance between the two transducers can be measured and the speed of sound in the water relates the distance and time measurements. Therefore, the speed of sound must be determined. The speed of sound was determined in two ways: first by fitting measured data in a least squares fashion and then by measuring the water parameters and using a well established speed of sound model. The speed of sound model estimate is used as the reference and the least squares fit of the data is compared to it as a measure of the system accuracy. The constant time bias associated with circuit delays and the uncertainty in the acoustic centres of the transducers is determined using both speed of sound estimates. Finally, the threshold locations and SNR levels are investigated for their effects on the time of arrival error.

4.1 Experimental Equipment

A pair of transducers were each mounted coaxially on the ends of 45cm rigid aluminum poles which in turn were each secured to adjustable carriages mounted on a 2m optical rail. It is not practical to measure the transducer separation in the tank as this would require underwater measurement; the separation must be measured in the air and the setup then lowered into the tank. Therefore the setup must be rigid so that the transducers do not move during the lowering process. The centre-to-centre separation of the two transducers can be easily measured to better than 1mm out of the tank and, even allowing for slight misalignments during the lowing procedure, the position as measured is confidently expected to reflect the true position to within $\pm$ 1mm.

4.2 Experiment 1 - Characterization

In order to characterize the toa system, any constant biases associated with circuit delays and the uncertainty of the transducers' acoustic centres must be determined. The relationship between the measured range and the estimated time of flight is

$$tof = \frac{R_{cc}}{v_{sound}} + t_{bias} \tag{4.1}$$

where R_{cc} is the measured centre-to-centre transducer separation, v_{sound} is the speed of sound in water and t_{bias} is the time bias associated with circuit delays, uncertainty of the transducers' acoustic centres, the effects of the threshold locations and SNR effects. The threshold location effects and the SNR effects must be kept to a minimum in order to isolate the constant time bias. As will be shown, this can be accomplished by keeping the ratio between thresholds and the peak of the envelope small and by keeping the threshold ratio V_R between 2 and 4. Maintaining a high SNR reduces noise effects on the measurements to a minimal level.

From (4.1), it can be seen that the speed of sound in water relates the time and distance measurements and therefore a value for the speed of sound is required in order to determine the constant time bias of the system. The speed of sound was determined in two ways: applying a least squares fit to the measured data and using the NRL II speed of sound model (del Grasso 1974). The least squares fit involves taking many data points and fitting them in a least squares fashion to (4.1), whereas the NRL II

speed of sound model requires only the measurement of the water parameters salinity, pressure and temperature. The model salinity parameter is set to zero for fresh water and the pressure was set to $0.05\frac{kg}{cm^2}$ appropriate for fresh water at a depth of 0.5m. The most sensitive parameter, temperature, is measured with a calibrated Oceans Sensors CTD before and after each set of measurements. Because the variations of the salinity, pressure and temperature in the tank are small, the NRL II speed of sound estimate should be accurate to within $\pm 0.6\frac{m}{s}$, corresponding to an uncertainty in the temperature measurement of $\pm$ 0.2 °C, and is taken as the reference value for the speed of sound. The comparison between the reference and the value obtained from the least squares fit provides a measure of the accuracy of the system.

In this experiment, the tof is measured while varying the range and keeping the TER $\equiv \frac{v_1}{V_p}$ fixed at a low value and the SNR fixed at a high level. As long as the TER is sufficiently small, V_R is between 2 and 4 and the SNR is kept high, their effects should be negligible as suggested by theory (Section 2.5) and confirmed by Experiment 2 (Section 4.3).

The two measured quantities, tof and R_{cc}, are used in a linear least squares fit of (4.1). A typical Least Squares Fit (Baird 1962) of the slope ($\frac{1}{v_{sound}}$) and the intercept (t_{bias}) is shown in Figure 4.1.

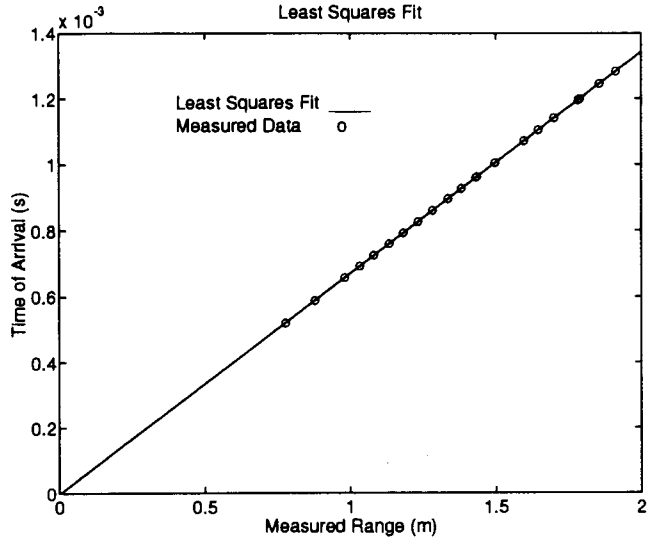

Figure 4.1: The least squares fit of the data to determine the speed of sound and the constant time bias.

On this scale the differences between the fit and the data is too small to be visible.

This experiment is performed with $v_1 = 0.1, v_2 = 0.4$ and varying the transducer separation between 1m and 2m. A comparison of the predicted speeds of sound using the NRL II model and the Least Squares Fit of (4.1) is shown in Table 4.1.

Table 4.1: Speed of Sound Estimates.

Speed of Sound $\left[\frac{m}{s}\right]$			
Experiment	NRL II Model	Least Squares Fit	
		Mean	σ
A	1488.49 ± 0.60	1487.67	0.47
B	1488.85 ± 0.60	1488.62	0.44
C	1488.45 ± 0.60	1487.84	0.60
D	1488.14 ± 0.60	1489.40	0.51
E	1488.08 ± 0.60	1488.17	0.41

The speed of sound measurements using both methods agree to within the errors. and thus gives confidence to the fitted time bias estimate. A difference in the speed of sound estimates of $1\frac{m}{s}$ implies a time uncertainty of 1.1μs.

The constant time bias is calculated in two ways: using the Least Squares Fit and using the model predicted speed of sound in (4.2). The results are shown in Table 4.2.

$$t_{bias} = tof - \frac{R_{cc}}{v_{NRLII}} \tag{4.2}$$

The measured constant time bias associated with circuit delays and uncertainty of the acoustic centres of the transducers agrees using both methods to within the errors. The COMBINED statistics are calculated using all the collected data from experiments A, B, C, D and E and they yield the mean time bias of -0.995μs with a standard deviation of 0.33μs.

The error in the time bias measurement can be compared with that predicted by theory. Errors are associated with the transducer separation measurement R_{cc}, in the parabolic fit estimation time, tof, and in the speed of sound prediction, v_{sound}. These sources of error are considered together to determine if the spread in the measured time bias data falls within the predicted theoretical error. Because the sources of

Table 4.2: Constant System Time Bias

Constant Time Bias [μs]				
Experiment	NRL II Model		Least Squares Fit	
	Mean	σ	Mean	σ
A	-0.91	0.32	-1.59	0.30
B	-1.10	0.29	-1.25	0.28
C	-1.11	0.40	-1.49	0.39
D	-0.91	0.30	-0.08	0.33
E	-0.84	0.18	-0.78	0.27
COMBINED	-0.995	0.33		

error are uncorrelated the absolute error in the time bias estimate can be represented as

$$\begin{aligned} \Delta t_{bias} &= \sqrt{\left(\frac{\partial t_{bias}}{\partial tof}\Delta tof\right)^2 + \left(\frac{\partial t_{bias}}{\partial R_{cc}}\Delta R_{cc}\right)^2 + \left(\frac{\partial t_{bias}}{\partial v_{sound}}\Delta v_{sound}\right)^2} \\ &= \sqrt{\Delta tof^2 + \left[\frac{1}{v_{sound}}\Delta R_{cc}\right]^2 + \left[\frac{R_{cc}}{v_{sound}^2}\Delta v_{sound}\right]^2} \end{aligned} \tag{4.3}$$

where Δtof is the error in the time of flight estimate due to errors in the parabolic fit. The parabolic fit error is considered in detail later. ΔR_{cc} is the error in measuring the transducer separation and is estimated to be $\pm$ 1m and $\Delta v_{sound} = \pm 0.6\frac{m}{s}$ is the error in the speed of sound prediction.

The tof is calculated from (2.20) of Section 2.5. There are uncertainties in v_1, v_2, t_1 and t_2 and because all the sources of error are uncorrelated the uncertainty in the tof is

$$\begin{aligned} \Delta tof &= \sqrt{\left[\frac{\partial tof}{\partial t_1}\right]^2 + \left[\frac{\partial tof}{\partial v_1}\right]^2 + \left[\frac{\partial tof}{\partial t_2}\right]^2 + \left[\frac{\partial tof}{\partial v_2}\right]^2} \\ &= \sqrt{\frac{V_R + 1}{\sqrt{V_R} - 1^2}\Delta t^2 + \frac{1}{4}\frac{(t_2 - t_1)^2\left[V_R + \frac{1}{V_R}\right]}{v_1{}^2(\sqrt{V_R} - 1)^4}\Delta v^2} \end{aligned} \tag{4.4}$$

where $V_R \equiv \frac{v_2}{v_1} = 4$. Δv is the uncertainty in setting the threshold levels and is estimated to be $\pm$ 10mV. Δt is the uncertainty in the threshold crossing times. For

a 2MHz clock, the uncertainty in the threshold crossing times is $\pm\frac{1}{2}T_{clock} = \frac{1}{4}\mu s$. $(t_2 - t_1)$ is the difference between the time when the lower threshold was crossed and the time when the upper threshold was crossed. This value depends on the threshold ratio and where on the rising edge the thresholds appear, but as seen from experiment a typical value is $10\mu s$. v_1 is the lower threshold level and in this case it was set to 0.1v. The tof error calculated using (4.4) is $1.17\mu s$.

Using the uncertainties

$$\begin{aligned} \Delta tof &= 1.17\mu s \\ \Delta R_{cc} &= \pm 1mm \\ \Delta v_{sound} &= \pm 0.6\frac{m}{s} \\ v_{sound} &= 1488\frac{m}{s} \\ R_{cc} &= 2m \end{aligned}$$

in (4.3) the theoretically predicted uncertainty in the time bias estimate is found to be $1.45\mu s$. This is the expected error in a single measurement with no SNR level effects or threshold location effects and from Figure 4.2 the spread in the measured time bias data of all the experiments can be seen to lie within the predicted error of $1.45\mu s$.

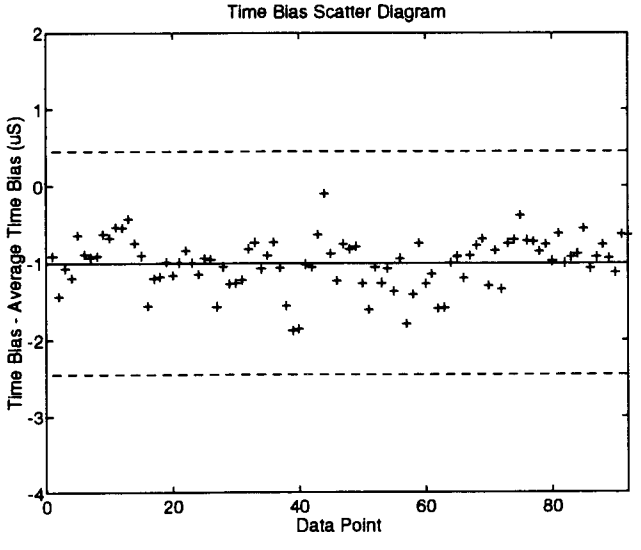

Figure 4.2: A scatter diagram of the time bias data.

The constant time bias, shown in Table 4.2, is negative which means, from (4.2), that the tof estimate is less than the measured transducer separation distance. From Table 4.2 the measured time bias is $\sim -1\mu s$. There are two possible sources for this time bias: circuit delays and an uncertainty in the acoustic centre of the transducers i.e. the question of whether or not the pressure wave originates from the centre of the transducer or from the surface of the ceramic.

The circuit delay of the receiver was measured directly using an oscilloscope. However the scope resolution was such that it was not possible to unambiguously determine the delay; the delay if any was less than $3\mu s$. The existence of an electronic delay would cause the tof estimate to be **greater** than the measured distance.

The transducer separation was measured center-to-center and the transducers have a radius of $\sim$ 6mm which corresponds to $\sim 4\mu s$ using $1488\frac{m}{s}$ as the speed of sound. If the pressure wave originated at the surface of the transducer the tof estimate would be **less** than the measured distance by $4\mu s$, if it originated at the centre of the transducer it would be zero.

The combination of an electronic delay and uncertainty in the position of the acoustic centre could give rise to a bias of anywhere between -4 and $+3\mu s$. Therefore the measured bias of $-0.995\mu s$ is reasonable.

Recall that the constant time bias was calculated here while maintaining a small TER ($\frac{v_t}{V_p}$) and V_R between 2 and 4 and a high SNR. Both the location of the thresholds and the SNR have added effects on the tof estimate and are investigated in the following experiments.

4.3 Experiment 2 - The Parabolic Assumption

The parabolic nature of the rising edge of the pulse and the effects of threshold selection need to be investigated using the toa system. The error produced as a result of the location of the thresholds on the rising edge is a measure of the validity of the parabolic approximation. The threshold levels were slid along the rising edge and the shape of the error curve is discussed with reference to the parabolic approximation. When the $TER \rightarrow 0$ the parabolic approximation is most valid and its effects are minimal. The constant time bias was measured as $TER \rightarrow 0$ and compared with that measured in Experiment 1 (Section 4.2).

A high SNR level was maintained throughout this experiment to isolate the effects of the parabolic assumption on the time of arrival error. The experiment was performed by sliding the threshold levels along the rising edge but maintaining their ratio constant. The experiment was repeated for four values of the threshold ratio, $V_R = 2, 3, 4$ and 5.

Using the NRL II model to estimate the speed of sound, as in Experiment 1, and the measured transducer separation the constant travel time can be removed from the time of flight and the constant time bias and prediction errors can be evaluated. The transducer separation is measured to be $R_{cc} = 1385.5mm \pm 1mm$ which corresponds to 930.9 μs using $v_{sound} = 1488.28\frac{m}{s}$.

The constant travel time is removed from the measured data, and the result is the error associated with the constant time bias and the parabolic assumption effects. The parabolic assumption effects are minimal when the TER is small, as determined in Section 2.5 and the constant time bias as $TER \rightarrow 0$ and found to be $t_{bias} \sim -0.90\mu s$ which is consistent with $t_{bias} = -0.995\mu s \pm 0.33\mu s$ found in Experiment 1 (Section 4.2).

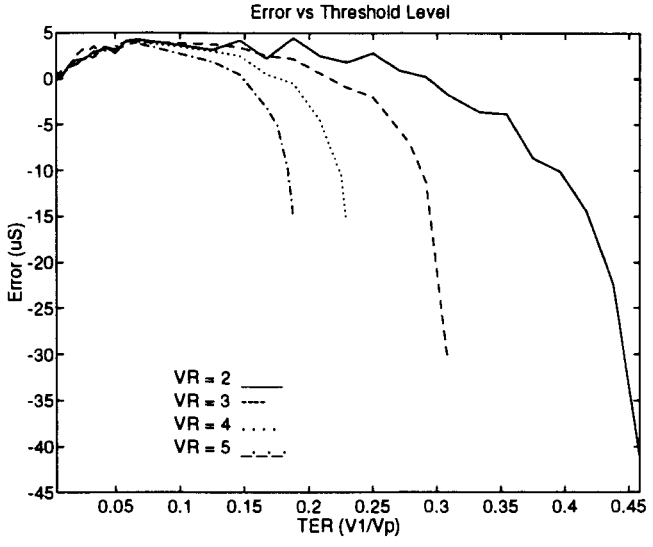

Figure 4.3: The parabolic nature of the rising edge of a toa pulse for various threshold ratios. The constant travel time and the time bias have been removed.

It can be seen from Figure 4.3, a plot of the tof versus the lower threshold level v_1 that the parabolic assumption is valid mostly in the lower portion of the rising edge.

As the thresholds slide up the curve they gradually leave the region where the parabolic terms in the time response dominate and enter the region where the higher order terms become more significant. In this region the curve rises more sharply and in order for the algorithm to fit the parabola the curvature term must be increased. For this reason, the algorithm predicts the start of the pulse to be after the pulse actually arrives.

Continuing up the rising edge, the curve eventually begins to flatten. In this region the parabolic assumption loses validity as well. In order to fit the parabola the curvature term must be decreased and the algorithm predicts the start of the pulse before the actual time of arrival. The flatter the pulse gets the farther from the true time of arrival the estimate becomes.

The errors start from zero and increase to a maximum of 4 μs then they start to roll off and become increasingly negative. There is a sharp rise in the error at low TER, then the error levels off before it dramatically increases in the negative direction near the knee of the pulse. The shape of the curves in Figure 4.3 is consistent with that predicted by the sampled pulse of Figure 2.10 of Section 2.5 even down to the sharp rise as can be in Figure 4.4, an enlarged scale version of Figure 2.10.

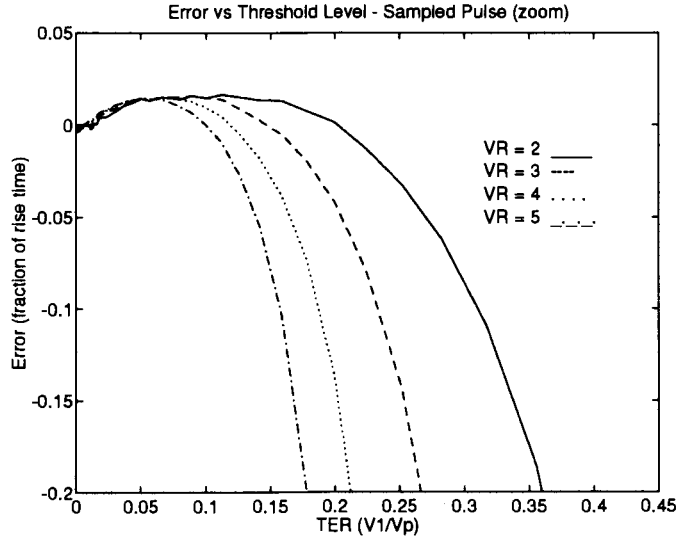

Figure 4.4: The parabolic nature of the rising edge of a toa pulse for various threshold ratios on a zoomed scale to display the sharp rise in error at low TER.

The curves shown in Figure 4.3 are typical of the results observed in similar experiments at different transducer spacings.

4.4 Experiment 3 - SNR Effects

In the previous experiment the SNR was maintained at a high level so as to minimize its effects on the threshold selection experiment. Now the effects of the SNR on the time of arrival error are investigated. The SNR is held constant with $V_R = 2$ and the TER was varied to give an idea of the effects of the parabolic approximation on the expected error. This experiment is repeated for various SNR levels to generate the family of curves shown in Figure 4.5.

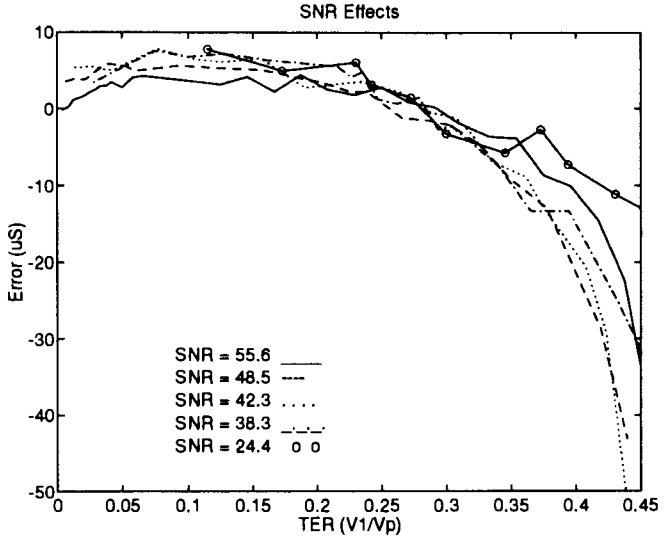

Figure 4.5: The SNR was set to various values between 24.35dB and 55dB and the TER was varied. The threshold ratio was maintained at $V_R = 2$. The constant travel time and the time bias are removed from the time of flight estimates.

The error in the figure is the time difference $(tof - \frac{R_{cc}}{v_{sound}} - t_{bias})$.

If a comparison is made between the noise free digitized pulse parabolic approximation curve for $V_R = 2$, shown in Figure 2.10 of Section 2.5, and the family of parabolic approximation curves for different SNR values of Figure 4.5, it can be seen that fitting the noise free curve to the data simply involves shifting it upwards by approximately $5\mu s$ indicating that the noise contribution to the system inaccuracy is,

in addition to the scatter observed about the noise free curve, a $5\mu s$ delay as can be seen in Figure 4.6.

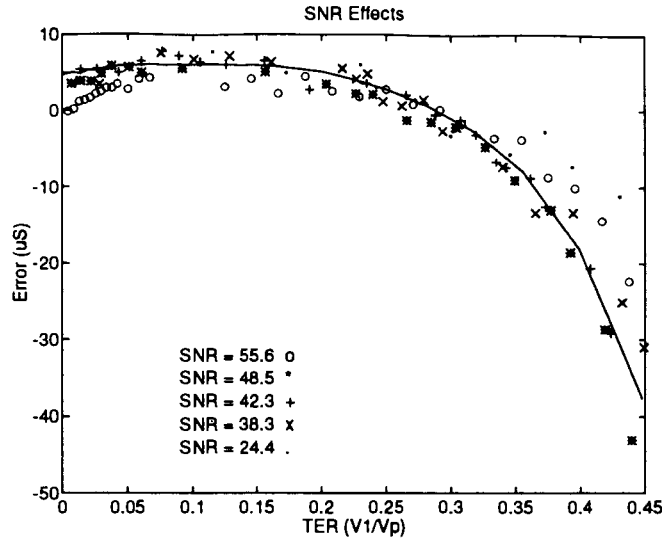

Figure 4.6: The SNR was set to various values between 24.35dB and 55dB and the TER was varied. The threshold ratio was maintained at $V_R = 2$. The constant travel time and the time bias are removed from the time of flight estimates. An offset of $5\mu s$ was added to the error predicted using the digitized pulse to compare with the family of SNR curves.

Careful examination of the figure shows that the delay is approximately independent of SNR and indicates the parabolic approximation holds very well over a wide range of SNR. It is important to note that that the 55dB data approaches zero error for small TER values, an effect consistently observed for high SNR values.

4.5 Noise

The noise level of the system needs to be determined in order to verify the theoretical predictions. The noise generated by the pre-amp was measured using a spectrum analyzer to integrate the noise over the bandwidth. The noise measured at the output of the bandpass filter was integrated and referred to the input of the pre-amp by dividing by the gain of the first two stages. Assuming a Gaussian noise distribution at the input of the pre-amp the rms noise was found to be $1.46\mu V_{rms}$. The measured noise level of $1.46\mu V_{rms}$ is close to the theoretically calculated value of $1.2\mu V_{rms}$.

The noise level at the output of the envelope detector depends on the gain through the receiver section; in this case it was set to 475. The rms noise voltage at the output of the envelope detector is found by multiplying the rms noise voltage at the input of the pre-amp by the receiver gain. The signal plus noise at the output of the envelope detector has a Rician distribution as was discussed in Section 2.6.3. For large signal levels the Rician distribution can be approximated as Gaussian with the same variance as the noise at the input of the pre-amp but with mean equal to the signal level (Middleton 1987). The peak to peak noise voltage expected from the pre-amp at the output of the envelope detector is found by multiplying the rms level by 6 (i.e. $\pm 3\sigma$) and is $4.16mV$. The noise measured at the output of the envelope detector was $18mV$ which is larger than the predicted $4.16mV$. The discrepancy appears to be a result of leakage from the transmitter and external devices such as personal computers and their monitors.

The ultimate goal of this thesis is to quantify the expected errors of the time of arrival estimates. To do this the expected SNR values and TER values must be determined.

First, the proposed criteria must be outlined. The system is expected to operate over a 100m range with transmit voltages of $\pm 60V_p$.

The relationship between the output envelope voltage, the transmit voltage and the range is found through the sonar equation (Urick 1983)

$$V_{RX}(dB) = SL + DI - TL - AL + OCV \tag{4.5}$$

where $V_{RX}(dB) = 10 \log {V_{RX}}^2$ is the level of the received signal at the output of the transducer without any amplification. The source level is the intensity of a plane wave produced by an acoustic source relative to the reference intensity. The source level takes into account the efficiency of the transducer and the efficiency of the signal waveform. The source level is

$$SL = 170.8 + 10 \log \left[\eta_{xducer} \eta_{waveform} \frac{{V_{TX}}^2}{R_{xducer}} \right] \tag{4.6}$$

where η_{xducer} is the efficiency of the transducer, $\eta_{waveform}$ is the efficiency of the waveform, V_{TX} is the peak transmit voltage and R_{xducer} is the impedance of the transducer.

The directivity index (DI) accounts for the fact that the source does not radiate isotropically. The transmission loss ($TL = 10\log R^2$ where R is the range) accounts for the loss in intensity due to spreading. The attenuation loss ($AL = -\alpha R$) accounts for the loss in intensity due to absorption. The open circuit voltage (OCV) is a measure of the receive sensitivity of the transducer.

In linear form, the sonar equation becomes

$$\begin{aligned} V_{RX} &= \frac{V_{TX}}{R}\sqrt{10^{17.08}\frac{\eta_{xducer}\eta_{waveform}}{R_{xducer}}10^{\frac{DI}{10}}10^{\frac{OCV}{10}}10^{\frac{-\alpha R}{10}}} \\ &= \frac{V_{TX}}{R}K \end{aligned} \tag{4.7}$$

The envelope level is the received voltage multiplied by the receiver gain and is

$$V_{env} = \frac{GV_{TX}}{R}K \tag{4.8}$$

where G is the receiver gain.

For the transducers used in this thesis the following parameters were determined.

$$\begin{aligned} \eta_{xducer} &= 0.3 \\ \eta_{waveform} &= \frac{8}{\pi^2} \\ R_{xducer} &= 600\Omega \\ DI &= 6.55 \\ OCV &= -205 \end{aligned} \tag{4.9}$$

The attenuation loss is a function of both the frequency of operation and the molecular properties of the medium. For a 125kHz signal operating in fresh water the attenuation loss is approximately zero for ranges < 100m.

Using the transducer specific parameters above the constant K of (4.7) is found to be $K = \sqrt{(660.5)10^{-9}}$.

The output envelope level received from a $60V_p$ transmit at a range of 100m with a gain $G = 475$ is $V_{out} = 0.23V$. Using the measured noise level of $18mV$, this corresponds to the minimum expected SNR of 22.13dB. Due to the uncertainty in setting the threshold levels, the lowest the threshold can confidently be set is ~ 50mV. With the envelope level at 230mV and the lower threshold set to 50mV, the TER is

~ 0.22. To account for any errors in estimating parameters the expected operating region will be taken as

$$TER \quad < 0.3$$
$$SNR \quad > 20dB$$

A $12\mu s$ wide band shown in Figure 4.7 spans the total spread in errors occurring as a result of $TER < 0.3$ and with $SNR > 20$dB.

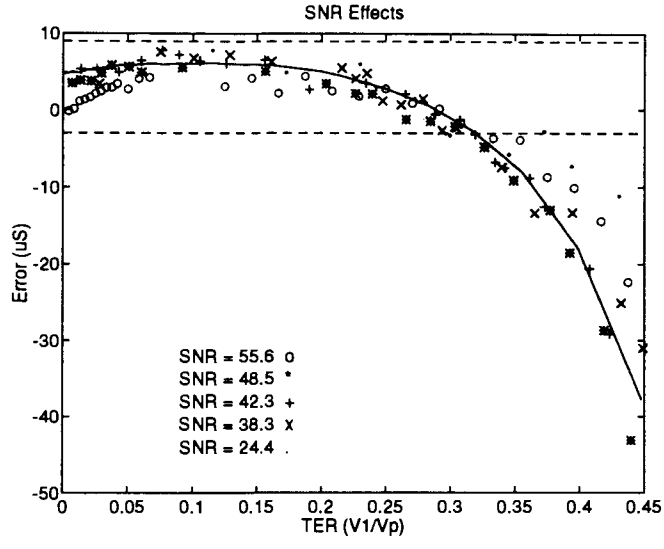

Figure 4.7: The expected operating region of the time of arrival system with a peak transmit voltage of $\pm 60V_p$ at a range of 100m. The lowest expected SNR is 22.13dB and the highest expected TER is 0.3 result in the operating region shown for $V_R = 2$ which gives an expected error of $\pm 6\mu S$ or 9mm.

Thus, there is a total timing uncertainty of $\pm 6\mu s$ corresponding to $\sim \pm 9$mm due to the combined effects of the parabolic approximation and the variation in SNR levels, which occur over the 100m range with a peak transmit voltage of $\pm 60V_p$.

As a final note, a comparison is made between the two point parabolic fit timing uncertainty and that of the simple threshold crossing technique. The simple threshold crossing technique, has estimate errors that vary from 0 to $28\mu s$ over the same operating range. The two point fit method proves to offer substantial improvements over the simple threshold crossing technique yet with little additional complexity.

Chapter 5

CONCLUSIONS

An underwater acoustic positioning system designed for use in a highly reverberant environment has been developed as an integral part of the SFU Underwater Research Laboratory AUV project. The heart of the positioning system is an acoustic pulse timing technique which fits the rising edge of an incoming pulse by using two threshold levels and their corresponding crossing times. The shape of the rising edge is dependent on the transfer function of the system involved. Although the pulses produced by this positioning system are found to have an almost parabolic rising edge, the technique described here can be applied equally well for any general system where the pulses rise as $a(t - t_a)^n$.

In order to characterize the time of arrival system an estimate of the quality of the predicted time of arrival was determined. Constant biases associated with the system as well as effects arising as a result of the parabolic approximation and varying SNR levels were evaluated. In evaluating the constant system bias a high SNR was maintained and the thresholds were held low relative to the peak envelope level as this was found to minimize their effects on the measurements. A constant time bias of $-0.995\mu S \pm 0.33\mu S$ was found to be associated with the uncertainty in the position of acoustic centres of the transducers and electronic circuit delays.

Investigations into the choice of threshold levels revealed that the best compromise between time of arrival errors and the range of allowable input signal levels was for a threshold ratio of between 2 and 4 and for a small TER value. The parabolic approximation was tested for SNR levels between 24dB and 55dB. The noise contribution to system inaccuracy was found to add a delay of about $5\mu S$ that was approximately

independent of noise indicating that the parabolic approximation holds well over a wide range of SNR levels.

The overall expected accuracy of the two point parabolic rising edge fit system over the expected operating range of 100m, with a peak transmit voltage of $\pm 60 V_p$, is $6\mu S$ corresponding to a range measurement accuracy of less than $1cm$. This is a substantial improvement over the simple threshold crossing technique, which yields errors in the time of arrival estimate that vary from 0 to $28\mu S$ over the same operating range, yet at a cost of very minor additional electronic complexity.

5.1 Future Work

System modifications can be implemented to attain additional improvements in the accuracy of the time of arrival estimate. By replacing the potentiometers currently used with more accurate digital voltage references the uncertainty in the threshold levels can be reduced. The timing resolution can be improved by reducing the clock period used in the timing counters, thus reducing the uncertainty in the threshold crossing times. Since most of the noise seen at the output of the envelope detector is probably the result of leakage from the transmitter and other external devices, a reduction in this noise could be realized with improved shielding around the receiver.

The transducers used in this thesis are not omni-directional and as a result their use in the positioning system will limit the region in which the positioning system can operate. Changing to omni-directional transducers will increase the operating region of the positioning system, but a decrease in the intensity of the pressure wave will occur as a result of the reduction in the directivity index and reduce the range of the system. The accuracy at greater ranges can be obtained by increasing the transmit voltage.

References

Analog Devices, I. (1992). *Amplifier Applications Guide.* Norwood, Mass.: Analog Devices Inc. Section XI - p21-31.

Anderson, L. (1979). Using error propagation methods to study various tracking algorithms. In *Proc. MTS IEEE Conf. Oceans*, pp. 519 – 524.

Baird, D. (1962). *Experimentation: an introduction to measurement theory and experiment design.* New Jersey: Prentice-Hall. Inc.

Barshan, B. and R. Kuc (1992, July/August). A bat-like sonar system for obstacle localization. *IEEE Transactions on Systems, Man, and Cybernetics 22*(4), 636 – 646.

Bobber, R. (1988). *Underwater Electroacoustic Measurements.* Los Altos, California: Peninsula Publishing.

Carnvale, A., M. Bowen, P.and Basileo, and J. Sprenke (1968, March). Absolute sound velocity measurement in distilled water. *Journal of the Acoustical Society of America 44*(4), 1098 – 1102.

Carpenter, R. and P. Stepanishen (1984, April). An improvement in the range resolution of ultrasonic pulse echo systems by deconvolution. *Journal of the Acoustical Society of America 75*(4), 1084 – 1090.

Christensen, J. (1979). Lbl nav - an acoustic transponder navigation system. In *Proc. MTS IEEE Conf. Oceans*, pp. 507 – 512.

Del Grasso, V. (1973). Tables of the speed of sound in open water (with mediterranean sea and red sea applicability). *Journal of the Acoustical Society of America 53*(5), 1384 – 1401.

Del Grasso, V. (1974, October). New equation for the speed of sound in natural waters (with comparisons to other equations). *Journal of the Acoustical Society of America 56*(4), 1084 - 1091.

Freitag, L. and P. Tyack (1993, April). Passive acoustic localization of the atlantic bottlenose dolphin using whistles and echolocation clicks. *Journal of the Acoustical Society of America 93*(4), 2197 - 2205.

Garrison, G., P. Kirkland, and S. Murphy (1961, March). Long-range measurement of sound speed in sea water. *Journal of the Acoustical Society of America 33*(3), 360 - 361.

Greenspan, M. and C. Tschiegg (1959, January). Tables of the speed of sound in water. *Journal of the Acoustical Society of America 31*(1), 75 - 76.

Lovett, J. (1978, June). Merged seawater sound speed equations. *Journal of the Acoustical Society of America 63*(6), 1713 - 1718.

Mackenzie, K. (1960, January). Formulas for the computation of sound speed in sea water. *Journal of the Acoustical Society of America 32*(1), 100 - 104.

Mackenzie, K. (1981, September). Nine-term equation for sound speed in oceans. *Journal of the Acoustical Society of America 70*(3), 807 - 812.

Marine Systems Engineering (1993, September). *Eighth International Symposium on Unmanned Untethered Submersible Technology*, Portmouth, NH. Marine Systems Engineering: Autonomous Undersea Systems Institute.

Medwin, H. (1975, December). Speed of sound in water: A simple equation for realistic parameters. *Journal of the Acoustical Society of America 58*(6), 1318 - 1319.

Middleton, D. (1987). *An Introduction to Statistical Communication Theory* (2 ed.). Los Altos, California: Peninsula Publishing.

Milne, P. (1983). *Underwater Acoustic Positioning Systems.* P.O. Box 2608 Houston, TX 77001, USA: Gulf Publishing Company.

Papoulis, A. (1984). *Probability, Random Variables, and Stochastic Processes* (2 ed.). New York, USA: McGraw-Hill Book Company.

Phillips, C. and R. Harbor (1988). *Feedback Control Systems.* Prentice-Hall Inc.

Stansfield, D. (1991). *Underwater Electronic Transducers.* Bath, U.K.: Bath University Press.

Treadwell, T. (1977). *Submersibles and Their Use in Oceanography and Ocean Engineering* (New York ed.). Elsevier Oceanography Series 17. Elsevier Scientific Publishing Company.

Ullate, L., M. Sanchez, E. Villanueva, and J. Anaya (1993). A three-transducer ultrasonic system for object location in air. *Sensors and Actuators A 37 - 38*, 391 – 396.

Urick, R. (1983). *Principles of Underwater Sound* (3 ed.). New York: McGraw-Hill Book Company.

Van Trees, H. (1971). *Detection, Estimation, and Modulation Theory Part III Radar-Sonar Signal Processing and Gaussian Signals in Noise.* Toronto: John Wiley and Sons Inc.

Waterloo Maple, S. (1981 - 1992). *Maple V Release 2.* Waterloo, Ontario: University of Waterloo.

Wilson, W. (1959, August). Speed of sound in distilled water as a function of temperature and pressure. *Journal of the Acoustical Society of America 31*(8), 1067 – 1072.

Wilson, W. (1960, June). Speed of sound in sea water as a function of temperature, pressure, and salinity. *Journal of the Acoustical Society of America 32*(6), 641 – 644.